Carnegie Mellon University

CARNEGIE INSTITUTE OF TECHNOLOGY

THESIS

SUBMITTED IN PARTIAL FULFILLMENT OF THE REQUIREMENTS

FOR THE DEGREE OF Doctor of Philosophy

TITLE   Rheology, Diffusion and Plastic

Correlations in Jammed Suspensions

PRESENTED BY   Arka Prabha Roy

ACCEPTED BY THE DEPARTMENTS OF

Civil and Environmental Engineering

Craig Maloney   August 31, 2015
ADVISOR, MAJOR PROFESSOR   DATE

David A. Dzombak   September 24, 2015
DEPARTMENT HEAD   DATE

APPROVED BY THE COLLEGE COUNCIL

Vijayakumar Bhagavatula   September 29, 2015
DEAN   DATE

Rheology, Diffusion and Plastic Correlations in Jammed Suspensions

Submitted in partial fulfillment of the requirements for
the degree of
Doctor of Philosophy
in
Computational Mechanics

Arka Prabha Roy

B. Tech., Mechanical Engineering, Indian Institute of Technology, Kharagpur

M. Tech., Thermal Science and Engineering, Indian Institute of Technology, Kharagpur

Carnegie Mellon University
Pittsburgh, PA

September, 2015

Acknowledgement

Abstract

We present results using Durian's bubble model [1] to study the spatio-temporal correlations and rheological response to imposed shear flow in steady state in jammed suspensions of soft, frictionless disks. We first study the so-called mean drag (MD) variant of the model which is appropriate for modeling particles at interfaces where the dominant dissipation comes from motion of the particle with respect to the phases off the interface. In this case, we find that the velocity fields are governed by a characteristic length, ξ, which scales with shear rate, $\dot{\gamma}$ like $\xi \sim \dot{\gamma}^{-1/3}$. Below ξ the velocity fields have the structure of uncorrelated Eshelby transformations. We find evidence for substantial alignment of the Eshelby transformations at all orientations, in contrast with the naive expectation that the sole contribution should come from transformations aligned with the imposed shear.

The finite time displacement fields become increasingly anisotropic at long lag times, Δt (or, equivalently applied shear strain, $\Delta \gamma$), and the correlations corresponding to the Eshelby transformations aligned along directions other than the principal shear directions become dominated by the correlations along the primary shear direction. The decay of correlations along the primary shear direction in real space becomes much slower for the displacements than the velocities. However, at any Δt, there is still a single characteristic length which scales the same way as the length scale encoded in the velocity fields. At the longest lag time, the structure factor of the displacement fields is consistent with results from athermal-quasi-static (AQS) simulations of conventional structural glasses with the power spectrum of the strain field, $S_\epsilon(\vec{k})$, decaying like $S_\epsilon \sim k^{-0.7}$.

We also measure the distribution of single-particle displacements in the gradient direction, $P(\Delta y)$ and its moments. The effective diffusion coefficient, $D_e = \lim_{\Delta\gamma\to\infty}\langle\Delta y^2\rangle/2\Delta\gamma = \lim_{\Delta\gamma\to\infty}\langle\Delta y^2\rangle/2\dot\gamma\Delta t$, scales with $\dot\gamma$ like $D_e \sim \dot\gamma^{-1/3}$. At low $\dot\gamma$, D_e saturates to a system size dependent quasi-static (QS) value, D_{QS} which scales with the length of the system, L, as $D_{QS} \sim L$. We can explain the relation between ξ and D_e by invoking an argument used to describe D_e in AQS of structural glasses. We also show that the macroscopic rheology follow a so-called Herschel-Bulkley (HB) law [2], $\delta\sigma = \sigma - \sigma_y = A\dot\gamma^\beta$ with $\beta \approx 1/3$ where σ is the shear stress, σ_y is the yield stress, and A is a constant. We find that an effective temperature defined as $T_{\text{eff}} = \delta\sigma D_e$ is essentially constant over several decades in $\dot\gamma$ and conjecture that the constancy of this effective temperature imposes a relation between D_e and $\delta\sigma$. At high $\dot\gamma$, $P(\Delta y)$, is surprisingly Gaussian at all $\Delta\gamma$, and there is a sharp cross-over from a ballistic to a diffusive regime.

Finally, we study the so-called pair drag (PD) variant of the bubble model using a form for the viscous drag which is appropriate for dissipation in a bulk suspension or emulsion rather than an interfacial assembly. In agreement with previous studies using the PD model [3], we find a HB exponent of $\beta \approx 1/2$. Here, we further show that the same basic connections between the displacement fields, single-particle displacement statistics, and rheology play out in the PD model in the same way as in the MD model. In particular, we find that $\xi \sim \dot\gamma^{-1/2}$, $D_e \sim \dot\gamma^{-1/2}$, and $\delta\sigma \sim \dot\gamma^{1/2}$ giving a constant value of $D_e\delta\sigma$ over several decades in $\dot\gamma$. The power spectrum of the displacement fields in the PD model for $k\xi >> 2\pi$ is remarkably similar to that of the MD model. For $k\xi \lesssim 2\pi$, the power in the displacement fields for the PD model is

essentially k independent, while for MD, it increases with k. We suggest that this is simply due to the fact that a linearized, continuum version of PD would damp all modes equally regardless of wavevector. Apart from this noise at long wavelength, the two drag models essentially give indistinguishable finite time displacement fields when compared at $\dot{\gamma}$ values which give equivalent ξ.

Contents

List of Figures

ix

Chapter 1

Introduction

1.1 Rheology of Jammed Suspensions

1.1.1 Jammed Suspensions

Suspensions of deformable particles are ubiquitous and are the building blocks of different everyday products such as food (ketchup, mayonnaise), personal care products (toothpaste, lotion, shaving cream), household goods (cement, paint) etc. All these materials have a common property – they can behave like a *solid* sustaining finite stresses, as well as a *fluid* flowing under the action of sufficient forces. These materials are known as "Yield stress fluids" or "Soft viscoplastic solids". These suspensions are composed of particles whose length scale varies from few nanometers to few hundreds of micrometers. Typical interactions energies are large compared to k_BT. They can be classified based on the particulate phase, as colloidal suspensions (solid particles submerged in liquid), emulsions (liquid drops in another immiscible liquid) and foams (air bubbles in liquid). Elastic forces and stresses in these systems arise from the *force network* created due to the persistent deformation of the particles at contact. Viscous forces and stresses arise from the shear induced in the suspending fluid when particles move relative to each other or relative to the background flow. These materials can resist a finite amount of applied stress before flowing like a viscous fluid above a particular yield stress, σ_y. The yield stress behavior is exploited in various industries to make different consumer products where it is often desirable for the materials to remain solid yet flow at low stress when desired (e.g. squeezing toothpaste through a tube or ketchup or mayonnaise through a bottle). The rheology

in steady flow can usually be described by Herschel-Bulkley (HB) model [2],

$$\sigma = \sigma_y + A\dot{\gamma}^{\beta} \tag{1.1}$$

where, σ is the flow stress, $\dot{\gamma}$ is the shearing rate, , and A and β are constants. β is also known as the HB exponent. The HB model accounts for the yield stress behavior as well as the non-linear viscosity observed in experiments.

Yield stress behavior in soft suspensions is observed particularly when the system is above the *jamming transition* or in a jammed state. The jammed state is obtained when the particles are confined volumetrically under compressive pressure such that they are forced to deform even when not sheared [12–16]. In this state the particles are in contact with most of its neighbors for finite duration of time and are confined by positive osmotic pressure. This so called jammed state [12, 13, 17, 18] can be achieved by increasing the density of these particles above the Random Close Packing (RCP) point [13].

In this work, we are interested in the regime where the characteristic energies associated with rearrangning a configuration of jammed particles are many many times $k_B T$. In such athermal systems, the particles can only move in response to external perturbations like imposed shear. The spontaneous thermal fluctuations are far too small to cause any particle rearrangements in the packings.
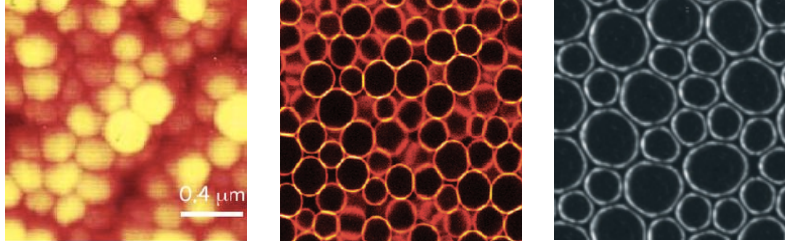
Figure 1.1: From left to right : Different kinds of jammed suspensions, (a) Concentrated microgel suspensions [4], (b) Oil-water emulsion (Blair Lab, Georgetown University), (c) Soap bubbles (Martin Van Hecke Laboratory, Leiden University)

1.1.2 Experimental Observations

In Fig. 1.1, we show optical images of some particular examples of the types of suspensions we are interested in. In the past few years many experimentalists [5–8, 19–26] have studied different classes of soft suspensions (soap bubbles, emulsions, microgel suspensions) in the unjammed as well as jammed state and generally found HB rheology. Here we discuss two typical types of rheology for the denser jammed packings– one for systems like soap bubbles and the another for micro-gel pastes and emulsions. The experimental results indicate that a major factor which determines the rheology is the geometry of the dissipation. In the case where the particles under shear live at an interface between two fluids (like soap bubbles at the air-water interface in a bubble raft), one finds an HB exponent of roughly 1/3. In the other case, where particles are sheared in bulk and the dominant source of drag should come from relative motion of particles, one finds an HB exponent of roughly 1/2.
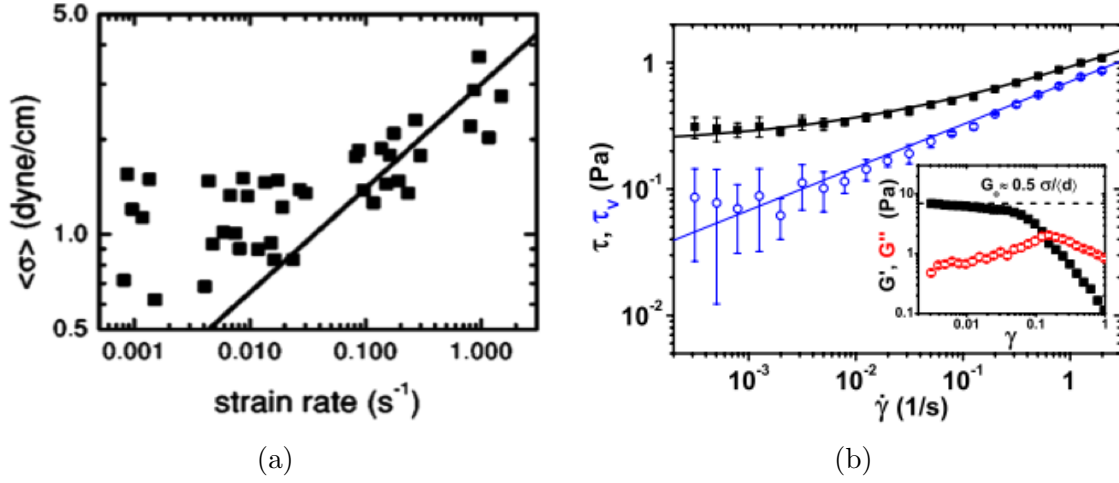
Figure 1.2: Foam rheology using bubble raft in 2D Couette cell. Results from (a) Pratt *et. al.* [5] and (b) Katgert *et. al.* [6]. The black line in (a) has a slope of 1/3 and the black curve in (b) is a Herschel Bulkley fit with an exponent of 0.36.

In 2003, Pratt *et. al.* [5] studied the rheology of a disordered wet foam. They observed yield stress rheology at slow shearing rates and reported an HB exponent of 1/3 for fast shearing rates (Fig. 1.2a). In Martin Van Hecke's group they performed similar bubble raft experiments using different geometries - from a freely floating monolayers of bubbles to confined bubbles with a glass plate on top [6, 19–21]. They found an HB exponent of 0.36 (Fig. 1.2b), roughly consistent with [5]. This type of bubble raft experiments are performed in a cylindrical coquette cell where single layer of disordered bubbles float on a water tank. The outer cylinder is the rotated and the resistive torque is measured at the inner cylinder. Majority of the resistive drag on the bubbles arrises due to the underneath flow field.
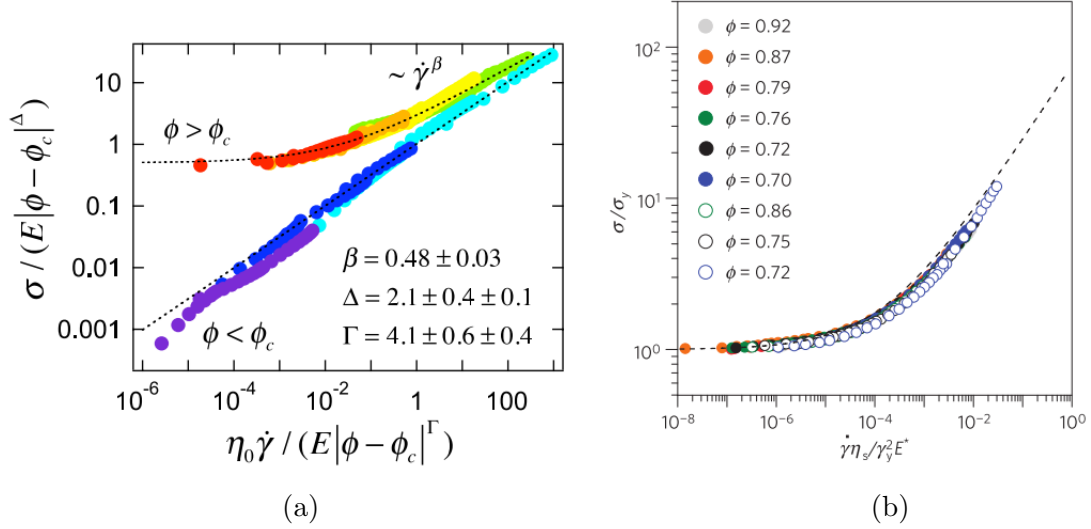
Figure 1.3: (a) Non-Newtonian rheology below jamming ($\phi < \phi_c$) and Yield stress behavior above jamming ($\phi > \phi_c$) in a microgel system [7]. Different colors correspond to different densities which are collapsed onto two master curves. (b) Scaled stress vs strain rate data for two different types of emulsion: high viscosity oil in water-glycerol (closed symbol) and low viscosity oil in water (open symbol). Dashed line corresponds to Herschel-Bulkley fit using the elasto-hydrodynmic model. [8]

Nordstrom *et. al.* [7, 24] studied the motion of dense microgel suspensions in a microfluidic rheometer for varying shearing rates. They observed different rheology on the two sides dependence on shearing rates at the two sides of jamming transition (Figure 1.3a). Above the jamming transition, the system developed a yield stress. Below jamming, the stress went to zero at zero shearing rate. But irrespective of packing fraction, at high $\dot{\gamma}$, the suspensions show a common power-law behavior with an exponent of 1/2. Langlois *et. al.* [3] studied the rheology using the Durian's bubble model [1] with drag forces proportional to the relative velocities of contacting particles. They showed the HB exponent to be 0.54, which was very close to the Nordstrom result [7]. In 2011, *Seth et. al.* [8] developed a detailed and relatively so-

phisticated elasto-hydrodynamic model for a paste composed of the same material as used by Nordstrom *et. al.* [7]. They also performed experiments on micro-emulsions with the minority phase fluid of varying viscosity. Their model equated the lubrication pressure at the gap between particles with the elastic pressure due to the Hertzian contact assuming that the particles were solid like object. They showed that this model also gave a HB rheology with an exponent of roughly 1/2 in agreement with the bubble model results of Langlois, and a fit for the two HB parameters, σ_y and A, resulted in an excellent fit to the data (Figure 1.3b).

1.1.3   Objective

In this work, we attempt to explain the observed rheology in both the interfacial (with HB exponent of 1/3) and bulk drag (with HB exponent of 1/2) scenarios by relating the macroscopic rheological response to the microscopic spatio-temporal correlations. Although others have reproduced the rheology in simulations for the bulk drag case [3, 8], here we differentiate ourselves by both performing an analysis of these spatio-temporal correlations to understand the rheology and also studying the interfacial drag case. We use discrete particle simulations in the athermal limit to study dense packings of deformable particles. The model we use [1] has repulsive harmonic interaction between particles and a simple damping force which models the viscous effect of the suspension at finite shear rates.

In particular, we want to answer the the question, "How are rheology, diffusivity, and spatial structure of the rearrangements related?" We will show that all three of these are governed by a single correlation length for the rearrangements which

7

diverges as the shearing rate vanishes in a way reminiscent of other athermal driven systems.

1.2 Amorphous Plasticity

1.2.1 Amorphous Solids

Amorphous materials do not have the crystalline structure of an elastic solid. Locally every site is different from every other site and stresses, energies, and other mechanical properties are broadly distributed. This is in sharp contrast to crystals. Despite having a broad distribution of local mechanical properties, at small load the response is elastic, similar to conventional, crystalline solids. Under applied shear some sites eventually yield and rearrange to accommodate the imposed shear. At low shearing rates, the response is bursty and intermittent, resembling other slowly driven out-of-equilibrium systems such as pinned elastic manifolds, Barkhausen noise in disordered ferromagnets, martensitic phase transformations, or dislocation-mediated crystal [27]. In recent years, it has become clear that shear flow in many types of amorphous solids – structural glasses such as metallic or polymer glasses; soft glasses such as pastes, emulsions, or foams; sheared granular matter – is governed by localized plastic shear transformations [28–32]. Like dislocation motion in a crystal, these shear transformations, or local rearrangements are the fundamental elementary process responsible for plasticity in an amorphous solid.

Bulatov and Argon [33–35] pointed out that the local rearrangements in amorphous media induce long-ranged strain fields [9,36–39], which redistribute the stress

8

in rest of the system. This load redistribution is precisely the same mechanism as in Eshelby's classical calculation of the stress increments in response to a local plastic transformation [36]. The Eshelby field corresponding to a single flip can be visualized in the far-field limit as the response due to two sets of force dipoles (Fig. 1.4a) acting at the origin in an infinite, elastic medium [9]. The force F can be determined using the dipole strength as $F = 2a\mu\Delta\epsilon_0$, where μ is the shear modulus, a is the length scale over which the flip occurs and $\Delta\epsilon_0$ is the eigen strain at the core. Assuming the stress developed due to the forces, $F/2a$ to be equal to the stress release at the core, $\mu\Delta\epsilon_0$ the displacement field $(r >> a)$ can be obtained as [40],

$$\vec{u} = \frac{a^2\Delta\epsilon_0}{2\pi}\frac{\sin 2\theta}{r^2}\vec{r} \tag{1.2}$$

(a) Force Dipole
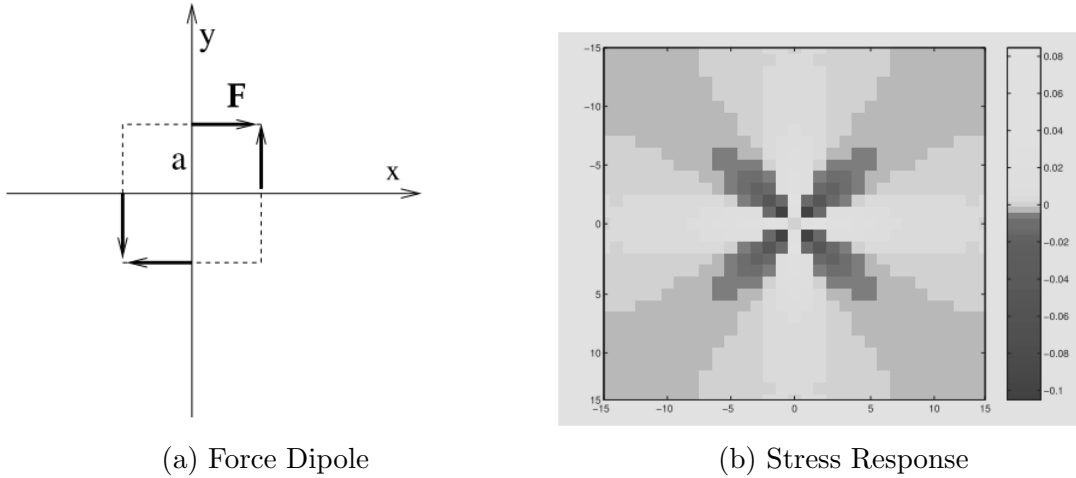
(b) Stress Response

Figure 1.4: (a) The perturbation due to a local plastic stress is equivalent to the perturbation due to the two set of force dipoles; (b) Response in stress field under the action of the force dipole. [9]

Simultaneously the shear-strain field can be calculated by taking the proper gradients [40],

$$\epsilon_{xy} = \frac{a^2 \Delta \epsilon_0}{\pi} \frac{\cos 4\theta}{r^2} \tag{1.3}$$

The quadrupolar symmetry in the shear stress response in Figure 1.4b reflects the angular anisotropy of the far field solution of shear strain according to equation 1.3.
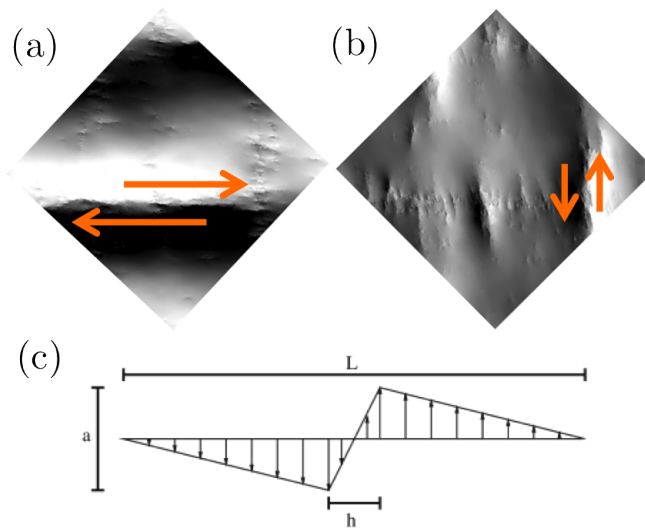
Figure 1.5: (a) Horizontal and (b) Vertical displacements during a horizontal slip event, (c) Schematic representation of the non-affine displacements parallel to a slip line of length L over a plastic zone of width h and a displacement discontinuity a. [10]

Maloney and Lemaitre [11] showed that in model metallic glasses, plastic events are composed of a series of local shear transformations that organizes into line of slips (Fig. 1.5). The slip lines are built up over the course of several successive avalanches. Eventually subsequent avalanches decorrelate from previous ones, and after this timescale, any given slip line is fully formed. In the quasi-static (QS) regime, this timescale for the decorrelation between successive avalanches is precisely

the same timescale required to build up a strain equal to the strain relieved by a single slip line. In Fig. 1.6, they show local Eshelby transformation in a molecular dynamics simulation of metallic glass. For the same Lennard-Jones glass, the long ranged strain correlations appear to be anisotropic and has strong correlations along the maximal shear stress direction [41].
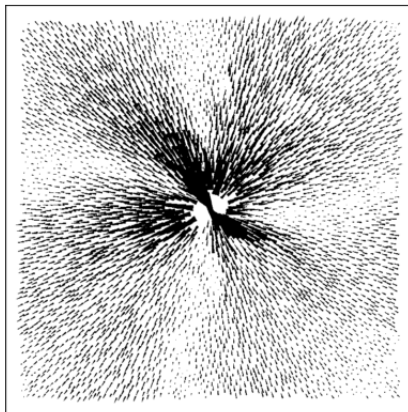
Figure 1.6: Non-affine displacement field at the onset of a plastic event in a metallic glass. Quadrupolar structure is the signature of an Eshelby flip event. [11]

1.2.2 Mean Field Models

Researchers have developed several mean field theories based on the idea of these localized yielding events. All these theories assume independent shear transformation, resulting deformation that depends only on the number of such local zones and their probability to yield. They explicitly neglect any correlations between transformations.

Modern studies of deformation in amorphous materials evolved from the works of Ali Argon [42] in the late 1970's and 1980's. Argon argued that plastic strain in

11

these materials arrises due to the balance of forward flips (releasing stress) and a *back flux*. According to him, flips of these weak areas in a substance are governed by an activation rate. This rate depends on the thermal activation energy needed for a zone to overcome the difference between free energy and elastic energy under an applied stress. In line with Argon's model, Falk and Langer [28] proposed the Shear Transformation Zone (STZ) theory, which states that deformation due to the flip of particular zones can be characterized by the dynamical state variable, number density of such zones. The idea of local flips or shear transformations has been supported by numerical simulations [11, 43–46]. Apart from these, there are other mesoscale models that describe the state of the system by probability distribution of *stress* level – Hebraud-Lequeux model (HL) model [47, 48] and *energy barrier* – Soft Glassy Rheology (SGR) [49, 50]. These models vary in their assumptions about the distribution of states, the barriers seen by the states, and the dynamics of the yielding events, but they all predict the HB type power-law rate dependence of the shear stress where $\sigma - \sigma_y = \delta\sigma \sim \dot{\gamma}^\beta$. However, the exponent, β, varies from model to model.

1.2.3   Elasto-plastic Models

One can, alternatively, construct explicit real-space models based on the notion of localized yielding events. These so-called elasto-plastic models (EPMs) were pioneered by Bulatov and Argon and many variations have been proposed in the intervening years [33, 35, 51–62]. These models, like the mean field theories, make assumptions about the distribution of states, barriers, rules and dynamics of yielding, and, im-

portantly, the dynamics of load redistribution after a local shear transformation. In most cases, with a few exceptions [51, 52], the loads are transferred instantaneously across all space as the site in question undergoes a yielding event. In one of the few EPMs where loads are transferred dynamically, a $\delta\sigma \sim \dot{\gamma}^{0.5}$ rheology was also observed [52]. Recently, Liu *et. al.* [63], have shown that in a rate dependent EPM, the rheology exhibits a crossover from a non-trivial universal scaling regime at low rate where $\delta\sigma \sim \dot{\gamma}^{0.65}$ to a mean field behavior at higher rate where $\delta\sigma \sim \dot{\gamma}^{0.51}$.

1.3   Dissertation Structure

This dissertation is organized as follows. In Chapter 2, we start with a description of the particle model explaining the two different dissipation mechanisms. We also discuss the simulation environment and the parameters used to perform the analysis. In Chapter 3, we present the rheology and instantaneous response for the Mean Drag (MD) version of the model. Detailed analysis of spatial correlation of velocity field for different shearing rates is demonstrated. We show interesting isotropic behavior of the overall velocity field. In Chapter 4, we examine the finite time displacement statistics, particle diffusion and the structure of the displacement field for the MD variant. A measure of effective temperature for this athermal soft suspensions is introduced to describe the connection between rheology and diffusion. In Chapter 5, we perform similar analysis as in Chapter 3 and 4, but for more sophisticated Pair Drag (PD) dissipation mechanism that take care of viscous forces due to individual particle-particle contact. We show that a single correlation length is responsible for

the diffusive behavior and an effective temperature can be constructed to explain the diffusion-rheology connection, similar to the other damping mechanism.

Chapter 2

Numerical Model

In this chapter we introduce the numerical model used to perform the particle based simulation. The important points to note here are:

1. All stresses come from persistent deformation at contact between the particles.

2. There is no thermal motion. If the system is not explicitly driven by external deformation, it will remain at rest.

3. The precise form of the repulsion between the interacting particles is not important. We use a harmonic repulsive contact force in the data reported here, but have observed similar behavior with non-linear contact forces such as Hertzian contacts.

4. The particles are modeled as perfectly circular disks, and there is no friction or adhesion/attraction at the contacts.

To study the dynamic behavior of the system we drive the system using a simple shear mechanism, under the assumption of overdamped dynamics, where the mass of the particles does not play a role .

2.1   Particle Scale Dynamics

We consider two dimensional system ($D = 2$) of soft disc like particles in a bi-disperse mixture to avoid crystallization [13]. Each particle i is defined by its radius R_i and has 2 time dependent parameters: its position $\vec{r_i}$ and velocity $\vec{v_i}$. $r_{ij} = |\vec{r_i} - \vec{r_j}|$ is the distance between the i-th and j-th particle. The particles can be thought as 2D discs that overlap on each other when the distance between them is less than the sum of

their radii, $r_{ij} < (R_i + R_j)$. The overlap is measured as, $\delta_{ij} = r_{ij}/(R_i + R_j) - 1$. There are N_L large and N_S small particles with $N_L : N_S = 50 : 50$. The size ratio of the particles are 1.4 [13], i.e., $R_L : R_S = 1.4 : 1$. All lengths are reported in units of the diameter of the smaller particle $D_S = 2R_S$.

$$U(r_{ij}) \propto \delta_{ij}^2$$
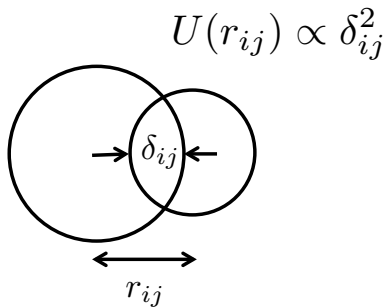
Figure 2.1: Repulsive Interaction between two disc like particles.

To study the dynamics of the collection of particles we follow the Durian's Bubble Model [1]. In this model, the particles experience two pairwise additive interactions based on their overlap and dissipative mechanism. First, the elastic repulsion is modeled by a harmonic potential $U = k\delta^2$ if $\delta < 0$ and zero otherwise, where k is the elastic spring constant between the particles. The elastic force on particle i due to particle j is,

$$\vec{F}_{ij}^E = -\frac{\partial U(r_{ij})}{\partial \vec{r}_j} \tag{2.1}$$

Thus, the total elastic force experienced by particle i due to its overlapping contacts j is,

$$\vec{F}_i^E = \sum_j \vec{F}_{ij}^E \tag{2.2}$$

The second interaction is the viscous dissipation which is taken into account in two

different ways.

Mean Drag (MD)

In this variant the dissipation occurs due to the relative velocity between the individual particle with respect to the average background flow. One can think this type of dissipation as the implementation of normal Stoke's Drag. This type of damping mechanism might be a realistic expression for the drag experienced by a soap bubble (or other deformable particle) floating on the surface of a deep tank of water [20, 64–67], where dissipative forces on a particle may be governed by the generated subsurface flow. In this case, the total drag force on particle i is,

$$\vec{F}_i^D = -b(\vec{v}_i - y_i \dot{\gamma} \hat{x}) \tag{2.3}$$

where b is the damping parameter, y_i is the location of the particle projected along the flow-gradient direction, $\hat{x}$ is the unit vector in the flow direction, and $\dot{\gamma}$ is the imposed shearing rate.

(a) (b)
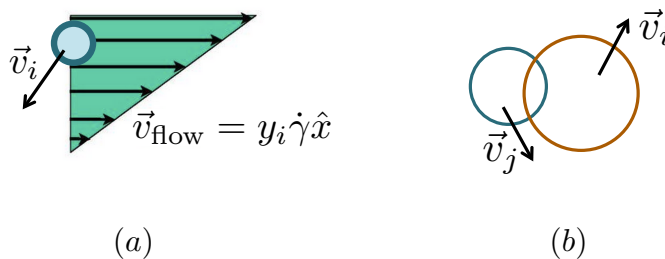
Figure 2.2: Two types of drag mechanism: (a) Mean Drag, (b) Pair Drag

18

Pair Drag (PD)

In this dissipation mechanism, drag force is proportional to the relative velocities of the particle with respect to its neighbors.

$$\vec{F}_i^D = -b \sum_j (\vec{v}_i - \vec{v}_j) \tag{2.4}$$

where j's are the particle indices for the neighbor of $i-$th particle. We call this mechanism, *Pair-Drag*, because the dissipation is modeled taking care of each pairwise contact. Important point to note is that in both dissipation mechanism the drag force is linear with the particle velocity. We then solve the Newton law of motion for each individual particle,

$$m_i \frac{d^2 \vec{r}_i}{dt^2} = \vec{F}_i^E + \vec{F}_i^D \tag{2.5}$$

where m_i is the mass of $i-th$ particle. As we are interested in the overdamped limit, mass can be considered negligible. For MD, replacing $m_i = 0$, we get the equation of motion for particle i,

$$\frac{d\vec{r}_i}{dt} = y_i \dot{\gamma} \hat{x} + \frac{1}{b} \sum_j \vec{F}_{ij}^E \tag{2.6}$$

In the case of PD, the mass is chosen small enough such that the system is overdamped. In this model the only relevant timescale is $\tau_D = \frac{b}{k}$. This is the characteristic relaxation time arising due to the competing mechanism for elastic storage and viscous dissipation. All subsequent times are reported in units of τ_D. In particular, the shear rate in subsequent sections is reported in units of $1/\tau_D$. In our simulations we have used $b = 1$ and $k = 1$.

2.2 Simulation Protocol
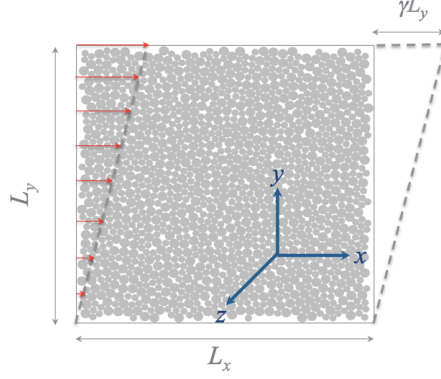
Figure 2.3: Primary Simulation cell in 2D space. Simple shear is applied along x direction.

We use the LAMMPS [68] molecular dynamics framework to perform the 2D numerical simulations. To integrate the equations of motion, a first order predictor corrector module has been written for LAMMPS with a time step, $\Delta t = 10^{-1}\tau_D$ for the MD model. We have confirmed the stability of our numerical scheme based on this time step for rates, $\dot{\gamma} \leq 10^{-3}$. For faster rates ($\dot{\gamma} > 10^{-3}$), we use smaller timesteps to avoid the numerical instabilities. For PD, we use $\Delta t = 0.05\tau_D$. Lees-Edwards boundary conditions [69] are used to implement the simple shear along x. We refer to the flow direction as x and the gradient direction as y. This is represented in Figure 2.4. Periodic images are replicated in x-direction and displaced periodic images are replicated in the y-direction according to the experienced shear. In this way we impose shear in a finite size simulation cell without boundary artifacts such as slip or structural ordering. Note however, the finite size of the cell could have an impact.
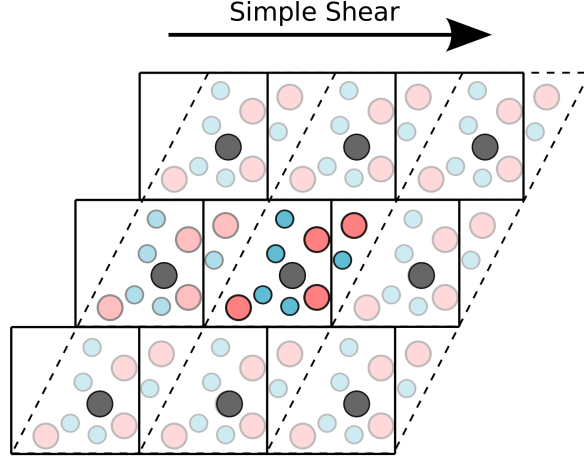
Figure 2.4: Strain Controlled periodic box with Lees Edwards boundary condition for a simple shear application.

Volume fraction, ϕ, is defined as $\pi(N_L R_L^2 + N_S R_S^2)/L^2$, where N_L and N_R are the number of large and small particles respectively, L is the simulation box size. As we are interested in the jammed state of the suspensions, we set the particle density, $\phi = 0.9$, which is above the jamming point, $\phi_J \approx 0.843$ in two dimension. We consider different sizes of the box for our simulations, $L = 40, 80, 160$ corresponding to a total number of, N equals to $1240, 4960, 19840$ particles. In this thesis we report steady state data, which is obtained beyond 50% of strain. Data accumulation and statistical analysis are performed between 50% to 150% strain.

Chapter 3

Instantaneous Response

In this chapter, we present the numerical results for the MD dissipation mechanism to illustrate instantaneous response of the system and explain how the structure of velocity field varies with increasing shear rate. But before going into the details of the velocity field, we evaluate the basic flow properties of the system under simple shear. We discuss the flow behavior in terms of macroscopic stress or *flow stress* which is measured as the average shear stress.

3.1   Macroscopic Stress

In the simple case of imposing a constant linear shear rate $\dot{\gamma}$ on the system, the shear stress σ_{xy} may be obtained from the usual microscopic Irving- Kirkwood definition [70],

$$\sigma_{\alpha\beta} = \frac{1}{L^2} \sum_{i=1}^{N} \left[\frac{1}{2} \sum_{j=1,i=1}^{N} f_{ij\alpha} r_{ij\beta} - m_i v_{i\alpha} v_{j\beta} \right] \tag{3.1}$$

where α, β represent the Cartesian coordinates, $\vec{r}_{ij} = \vec{r}_j - \vec{r}_i$, f_{ij} is the force exerted by on j-th particle on i and v_i is the velocity of i-th particle. For our bubble model, we use $m = 0$. Note that we exclude the contribution from the viscous forces which is negligible in the regime of shearing rates studied here.

3.1.1   Stress Response at Various Rate

When an amorphous material is driven slowly, majority of its time is spent loading elastically with little dissipation and a minority of its time is spent undergoing large plastic dissipation. This behavior of bursty energy dissipation during slow loading is seen in a many diverse systems including dislocation bursts in crystal plasticity

23

[71–74], domain wall motion in disordered magnets [75–77] and in amorphous solids like our model [78–82]. In the slow shear limit, the events are well separated from each other and occurs after a period of elastic loading. In Fig 3.1, we plot the shear stress, σ_{xy} vs. strain, γ for 3 different rates. At $\dot{\gamma} = 10^{-6}$, one can clearly observe the huge stress drop due to distinct particle rearrangement events (around $\gamma = 1.23$ in Fig 3.1) which are followed by several ramps of elastic loading [11,44,45]. As we increase the shearing rate, the system does not have enough time to relax after an event and the events start to overlap in time. Stress fluctuations for fast rates are suppressed compared to the slow rate. At very fast shearing rates ($\dot{\gamma} = 10^{-2}$), the relative fluctuations in stress are very small and the burstiness completely disappears..
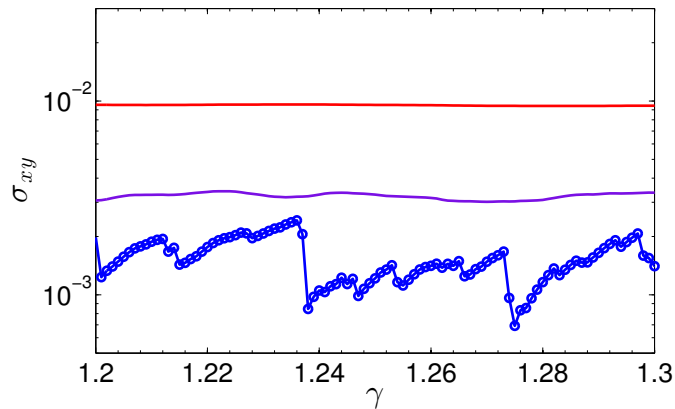
Figure 3.1: σ_{xy} vs. γ for different strain rates $\dot{\gamma} = 10^{-6}(blue), 10^{-4}(purple), 10^{-2}(red)$ for $L = 40$.

3.1.2 Rheology

By definition, 'Rheology' is the study of flow properties of liquids and soft materials under the condition where the response to applied stress is plastic in nature instead of
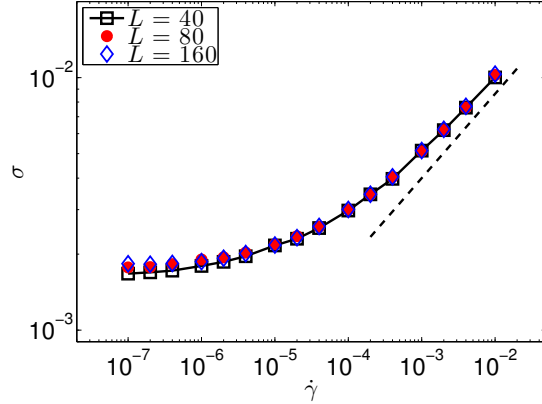
Figure 3.2: σ vs. $\dot{\gamma}$ for $L = 40, 80, 160$. The bold dashed line has a slope of $1/3$.

the well known elastic behavior of matter. For a linear elastic solid the deformation is proportional to the applied stress in small deformation limit and is governed by the Hooke's law, $\gamma = G^{-1}\sigma$, where G is the shear modulus. Above σ_y the material deforms permanently due to plasticity. On the other hand, most of the familiar liquids follow Newtonian behavior, $\sigma \propto \dot{\gamma}$; or in other words normal Newtonian liquids have a constant viscosity $\eta = \sigma/\dot{\gamma}$. The type of material we are interested in shows dual characteristics of solid as well as fluid at the dense state and followed HB behavior, $\delta\sigma = \sigma - \sigma_y \sim \dot{\gamma}^{\beta}$. It is also known, that as we approach the quasi static (QS) limit, the viscosity, η diverges with shear rate as $\eta \propto 1/\dot{\gamma}$. In Fig. 3.2, we plot the σ vs. $\dot{\gamma}$ for 3 different system sizes, $L = 40, 80, 160$ at a packing fraction of $\phi = 0.9$. We observe that σ does not depend on L. Irrespective of L, at vanishing rates one approaches the same yield stress (σ_y). At higher rates, one approaches a power-law regime which is described reasonably well by Eqn.1.1 with $\beta = 1/3$ for over a decade. We cannot rule out a cross-over to a different behavior at very low rates as one approaches the QS limit.

3.2 Non-affine Velocity

In the QS limit, stress fluctuates about yield stress as the system experiences large spatio-temporal fluctuations and shows intermittent behavior. As energy is injected smoothly by the applied strain, it dissipates in discrete bursts. But with increasing rate, the intermittency disappears and the stress fluctuations are minimized. In the first part of this section, we study the distribution of velocities[1] to discuss energy dissipation at various rate. In the later part we focus on the spatial correlations of the velocity field and the nature of the instantaneous structure of it.

3.2.1 Energy Dissipation and Velocity Distribution

In the MD model, we can define energy dissipation rate, Q, as the difference between the power input due to the applied deformation, $\sigma\dot{\gamma}$,[2] and time derivative of the total potential energy dU/dt,

$$Q = \sigma\dot{\gamma} - \frac{dU}{dt} \tag{3.2}$$

Time derivative of energy can be written as,

$$\frac{dU}{dt} = \left.\frac{\partial U}{\partial \gamma}\right|_s \dot{\gamma} + \sum_i \frac{\partial U}{\partial \vec{s_i}}\dot{\vec{s_i}} = \sigma\dot{\gamma} - \sum_i \vec{F_i^E}.\delta\vec{v_i} \tag{3.3}$$

where, $\vec{s_i}$ is the position of the i-th particle in co-moving reference frame, δv_i is the non-affine velocity and $\vec{F_i}$ is the total force on particle i due to the harmonic springs

---

[1] All velocities are the non-affine velocities defined with respect to background average flow, $\delta v_i = v_i - <v>$

[2] σ is the total virial (extensive) rather than the stress (intesive)

26

attached to it. $\left.\frac{\partial U}{\partial \gamma}\right|_s \dot{\gamma}$ can be identified as the applied work, $\sigma\dot{\gamma}$. Combining equations 3.2 and 3.3 we can get the expression for the instantaneous dissipation rate Q,

$$Q = \Gamma\dot{\gamma} = \sum_i \vec{F_i^E}.\delta\vec{v_i} = b\sum_i \delta v_i^2 \qquad (3.4)$$

Γ being the energy dissipated per unit strain and b, the drag coefficient. Important point to note, the total energy dissipated over all events occurring over a time interval equals the total stress times applied strain during that cycle. Whenever there is a big plastic rearrangement in the system the energy dissipation is huge. In Fig. 3.3, we plot the probability distribution of Γ for different $\dot{\gamma}$ for $L = 160$ in a log-log scale. At $\dot{\gamma} = 10^{-7}$, broad distribution of Γ can be understood as the interplay between long period of elastic loading and infrequent huge plastic dissipation when Γ is huge. In this low-rate regime, the Γ distributions are governed by the sum rule that the average Γ must be equal to the yield stress. With increasing $\dot{\gamma}$, Γ distributions get narrower and the $\langle\Gamma\rangle$ shifts right as σ increases.
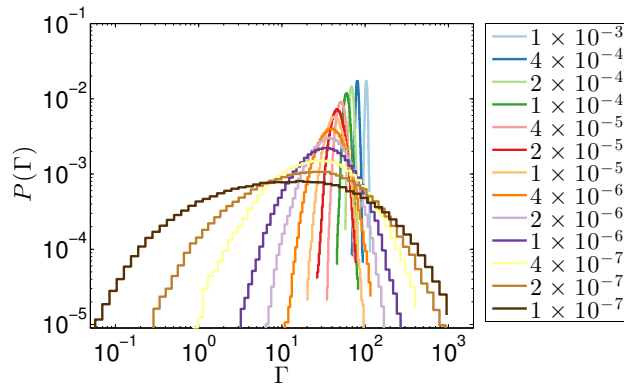
Figure 3.3: Probability distribution of Γ for different $\dot{\gamma}$, $L = 160$.

For an non-interacting, equilibrium system, velocity follows a Maxwell-Boltzmann

distribution with an width that depends on the temperature and mass of the particles. Our system is athermal but the dynamics is based on the dissipative particle rearrangements which gives rise to the non-affine velocities. Γ distributions tells us about the overall behavior of the dissipation and highlights the intermittency at low rates. We are also interested in the distribution of the particle velocities. In Fig. 3.4a we show the probability distribution of non-affine y-velocities for different rates. We observe as $\dot{\gamma}$ decreases the distributions become narrow. For slow rates where σ approaches σ_y, we observe power-law like velocity distributions with cutoffs at high velocities. For $\dot{\gamma} \geq 10^{-6}$, the crossover from plateau value follows $\dot{\gamma}^{-1}$, which suggests a rate dependent velocity scale. In Fig. 3.4b we plot the same distributions as in Fig. 3.4a, scaled by $\dot{\gamma}^{2/3}$ for $\dot{\gamma} \geq 10^{-6}$. The collapse of the crossover (at $v_y/\dot{\gamma}^{2/3} \approx 10^{-1}$) agrees with the overall scaling of dissipation rate, $\Gamma \sim \sigma \propto \dot{\gamma}^{1/3} \Rightarrow \langle \delta v^2 \rangle / \dot{\gamma} \propto \dot{\gamma}^{1/3} \Rightarrow \delta v \propto \dot{\gamma}^{2/3}$.

(a) $P(v_y)$ (b) $P(v_y/\dot{\gamma}^{2/3})$
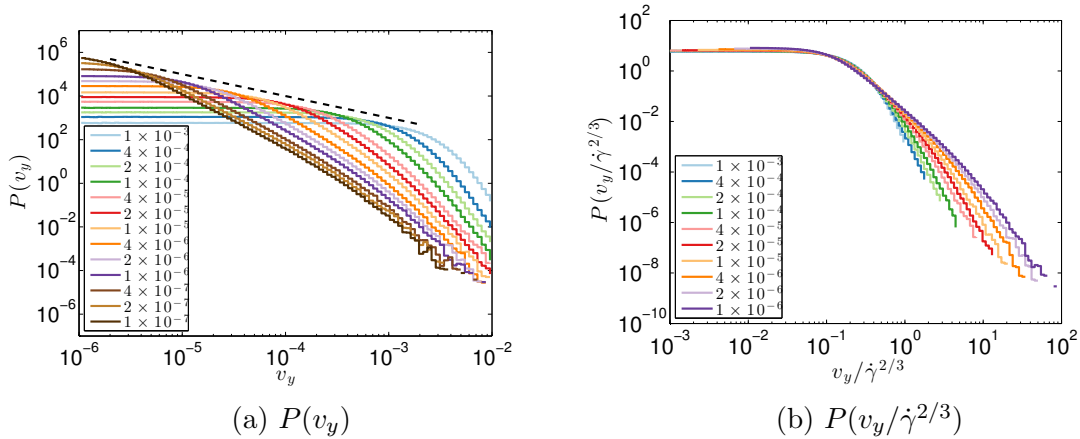
Figure 3.4: (a) Probability distribution of non-affine y-velocities for different $\dot{\gamma}$, $L = 160$. The bold dashed line has a slope of -1. (b) Distribution of v_y scaled by $\dot{\gamma}^{-2/3}$ for intermediate rates $\dot{\gamma} \geq 10^{-6}$, $L = 160$.

3.2.2 Emerging Correlation Length, $\xi \propto \dot{\gamma}^{-1/3}$
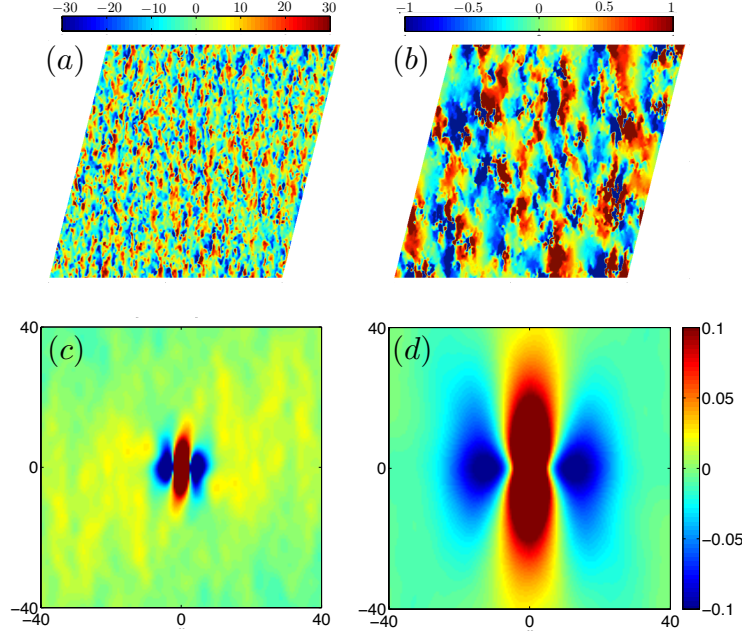
Figure 3.5: Top: A typical map of $10^4 v_y$ for (a) $\dot{\gamma} = 10^{-3}$ and (b) $\dot{\gamma} = 10^{-5}$ using $L = 160$. Bottom: Spatial autocorrelation of y-velocities $C_{v_y}(\vec{R})/C_{v_y}(x = 1)$ for (c) $\dot{\gamma} = 10^{-3}$ and (d) $\dot{\gamma} = 10^{-5}$.

To understand the the nature of the particle rearrangement spatially we first study the spatial correlation of velocity field. We define spatial autocorrelation function for v_y as,

$$C_{v_y}(\vec{R}) = \langle v_y(\vec{R} + \vec{r}, t) v_y(\vec{r}, t) \rangle_{(\vec{r}, t)} \tag{3.5}$$

In Fig. 3.5, we plot a typical snapshot of v_y field at two typical rates, (a) $\dot{\gamma} = 10^{-3}$ and (b) $\dot{\gamma} = 10^{-5}$, and their respective time-averaged spatial autocorrelation functions, C_{v_y}, in (c) and (d). The large coherent spatial structures are obvious. These correspond to long lines of particles which are all slipping together *at the same*

instant. The sharp jumps from blue to red as one traverses the image from left to right indicate discontinuities in the velocity field with counter-clockwise vorticity. The real-space correlation functions reflect the visual impression. The y-velocities have strong correlations along the y direction. They are correlated along the x-direction for some distance and eventually become anti-correlated. One would naturally associate the cross-over from correlation to anti-correlation with the typical spacing between the slip lines.
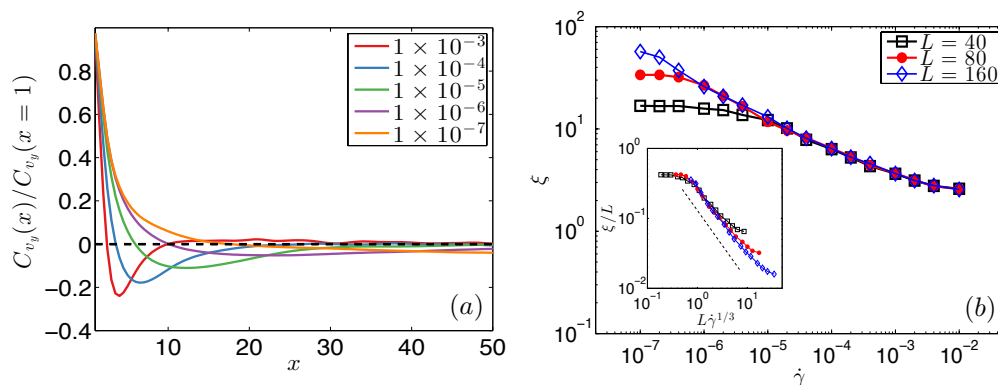
Figure 3.6: (a) $C_{v_y}(R = x)/C_{v_y}(x = 1)$ for different $\dot{\gamma}$, $L = 160$. The bold dashed line shows zero correlation. (b) ξ vs. $\dot{\gamma}$ for different L. Inset: ξ/L vs. $L\dot{\gamma}^{1/3}$. The bold dashed line has a slope of -1.

In Fig. 3.6a, we plot the traces of C_{v_y}, along the x-separations, normalized by the $x = 1$ values, for various shearing rate for $L = 160$. In Fig. 3.6b, we plot the location, ξ, of the minima of each C_{v_y} curve as a function of rate for various system size. For $L = 40$ and 80, we see a clear QS plateau at the lowest rates where ξ saturates near the system size, while the $L = 160$ system is just starting to show system-size dependent behavior at the lowest rate. At higher rates, the data is well described by a $\xi \sim \dot{\gamma}^{-1/3}$ power law. There are deviations from scaling in the high

$\dot{\gamma}$, small ξ regime, below about $\xi \approx 5$. Nonetheless, we can observe over a decade of scaling for the $L = 160$ system. In the inset, we plot ξ/L vs $L\dot{\gamma}^{1/3}$ showing the $\xi_{QS} \sim L$ quasi-static scaling. The data cannot rule out a $\log L$ correction.
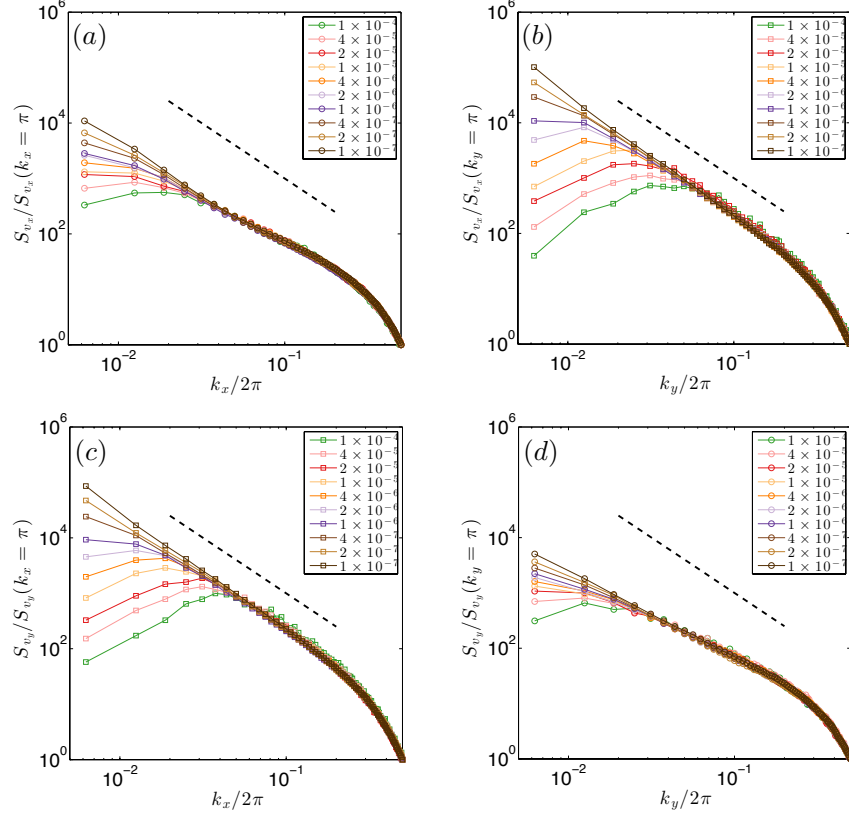
Figure 3.7: (a) S_{v_x} along k_x, (b) S_{v_x} along k_y, (c) S_{v_y} along k_x and (d) S_{v_y} along k_y for different strain rates. The bold dashed lines have slopes of -2.

Next, we focus on the velocity correlation in fourier space. We calculate the power spectrum, $S(\vec{k})$ which gives the intensity as a function of the wave-vector, $\vec{k}$ [see Appendix C for the calculation]. In Fig. 3.7a and 3.7b, we plot the power of x-velocities, S_{v_x} normalized by the power at 2 particle distance along longitudinal (k_x) and transverse (k_y) direction respectively for various rates. Similarly in Fig. 3.7c and

31

3.7d, we plot the power of y-velocities S_{v_y} along transverse (k_x) and longitudinal (k_y) direction respectively for different rates. With increasing $\dot{\gamma}$ there is a development of peak whose location shifts to increasing k, which is clearly visible in the plots along the transverse directions (in Fig. 3.7b and 3.7c). Irrespective of $\dot{\gamma}$, transverse power shows k^{-2} behavior at intermediate wavelengths before falling off for faster rates at long wavelength limit. This k^{-2} dependence can be explained by the simultaneous occurrence of several spatially uncorrelated *Eshelby* flips. It is surprising to see that longitudinal power (in Fig. 3.7a and 3.7d) is relatively less sensitive to $\dot{\gamma}$, compare to transverse power.
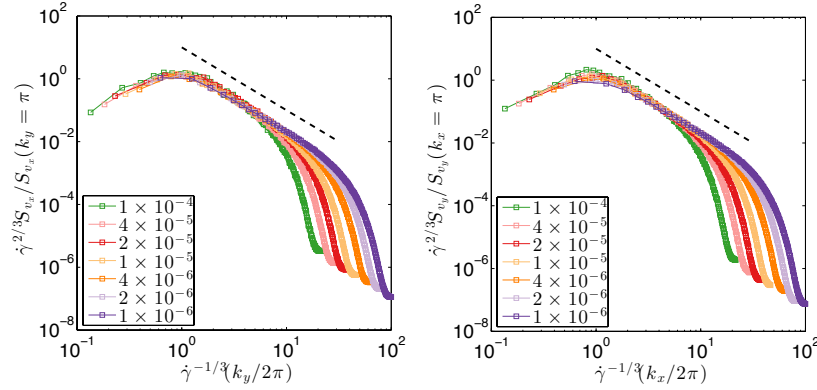
Figure 3.8: Left: Normalized S_{v_x} along cuts of k_y scaled by $\dot{\gamma}^{1/3}$, Right: Normalized S_{v_y} along cuts of k_x scaled by $\dot{\gamma}^{1/3}$. The bold dashed lines have slopes of -2.

In Fig. 3.8, we show S_{v_x} and S_{v_y} along their respective transverse directions (as in Fig. 3.7b and 3.7c) scaled by $\dot{\gamma}^{\alpha\beta}$ vs. $\dot{\gamma}^{-1/3}(k_y/2\pi)$ and $\dot{\gamma}^{-1/3}(k_x/2\pi)$ respectively, where $\alpha = -1/3$ and $\beta = -2$. The data collapse for rates, $10^{-6} \leq \dot{\gamma} \leq 10^{-4}$, suggests the emergence of a rate dependent correlation length. This result agrees with $\xi \sim \dot{\gamma}^{-1/3}$ behavior obtained from the real space transverse correlation[Fig. 3.7(b)].

3.2.3   Structure of Velocity Field

We next present an exhaustive study of the structure of the instantaneous response by looking at the velocity gradients[3]. The strain-rate tensor in two dimension can be expressed as,

$$\nabla v = \begin{bmatrix} \partial_x v_x & \partial_y v_x \\ \partial_x v_y & \partial_y v_y \end{bmatrix} \tag{3.6}$$

Instead of studying the individual components of the strain-rate tensor we look at some particular combinations of these, which are relevant to understand shear deformation. In simple shear geometry, principal stress directions lie along the diagonals, θ equals to $\pi/4$ and $3\pi/4$. And the maximal shear happens along the horizontal, $\theta = 0$ and vertical, $\theta = \pi/2$ directions. As a result, shear deformations are dominated by forming vertical and horizontally aligned transient slip lines [11].

In Fig. 3.9 we show typical snapshots of different measures of strain-rate, from left to right, $\dot{\epsilon} = (\partial_x v_y + \partial_y v_x)/2$, $\dot{\Psi} = (\partial_x v_x - \partial_y v_y)/2$ and $\dot{\omega} = (\partial_y v_x - \partial_x v_y)/2$ for 3 shearing rates, from top to bottom, $\dot{\gamma} = 10^{-4}, 10^{-5}, 10^{-6}$. With decreasing $\dot{\gamma}$, we can observe the emergence of long ranged vertical and horizontal slip lines in the $\dot{\epsilon}$ field. We can also observe small slips along the $\pi/4$ and $3\pi/4$ direction in $\dot{\Psi}$ fields, which is surprising. $\dot{\omega}$ fields have more isotropic behavior compare to the $\dot{\epsilon}$ and $\dot{\psi}$ fields, but the horizontal slip lines (white line in Fig. 3.9c,f,g) can be seen analogous to the $\dot{\epsilon}$ field (in Fig. 3.9a,d,g).

In Fig. 3.10, we plot the time averaged spatial auto correlation function for $\dot{\epsilon}$, $\dot{\Psi}$ and $\dot{\omega}$ for the same rates, $\dot{\gamma} = 10^{-4}, 10^{-5}, 10^{-6}$. The angular variation in $\dot{\epsilon}$ correla-

---

[3]Details about the gradient calculation is explained in Appendix. B
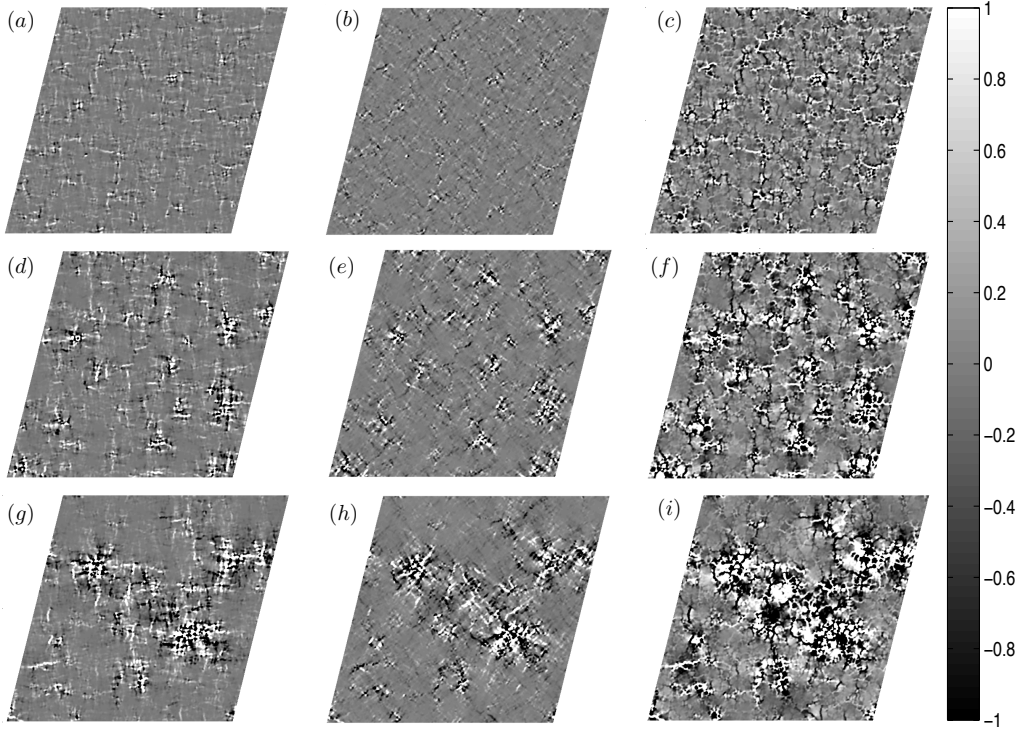
Figure 3.9: Typical maps for $\dot{\epsilon}$, $\dot{\Psi}$ and $\dot{\omega}$ for 3 different rates, **Top row :** $\dot{\gamma} = 10^{-4}$ (a)$10^3 \times \dot{\epsilon}$, (b)$10^3 \times \dot{\Psi}$, (c)$10^3 \times \dot{\omega}$, **Middle row :** $\dot{\gamma} = 10^{-5}$ (d)$10^4 \times \dot{\epsilon}$,(e)$10^4 \times \dot{\Psi}$,(f)$10^4 \times \dot{\omega}$, **Bottom row :** $\dot{\gamma} = 10^{-6}$(g)$10^5 \times \dot{\epsilon}$, (h)$10^5 \times \dot{\Psi}$, (i)$10^5 \times \dot{\omega}$ for $L = 160$.

tions has a quadrupolar symmetry reminiscent of the strain fields one would obtain from uncorrelated Eshelby transformations [83] with strong correlations along the directions of maximum shear and strong anticorrelations 45 degrees away. For increasing $\dot{\gamma}$ the correlations are cutoff at shorter lengths, which is evident as we go up from $\dot{\gamma} = 10^{-5}$ (Fig. 3.10d) to $\dot{\gamma} = 10^{-4}$ (Fig. 3.10a). $C_{\dot{\Psi}}$ has similar quadrupolar pattern as $C_{\dot{\epsilon}}$ with positive correlations along the 45 degrees. For $L = 160$, $C_{\dot{\Psi}}$ has less dependance on rate compare to $C_{\dot{\epsilon}}$. On the other hand although $C_{\dot{\omega}}$ look more isotropic than $C_{\dot{\Psi}}$ and $C_{\dot{\epsilon}}$, anisotropy increases with increasing $\dot{\gamma}$.
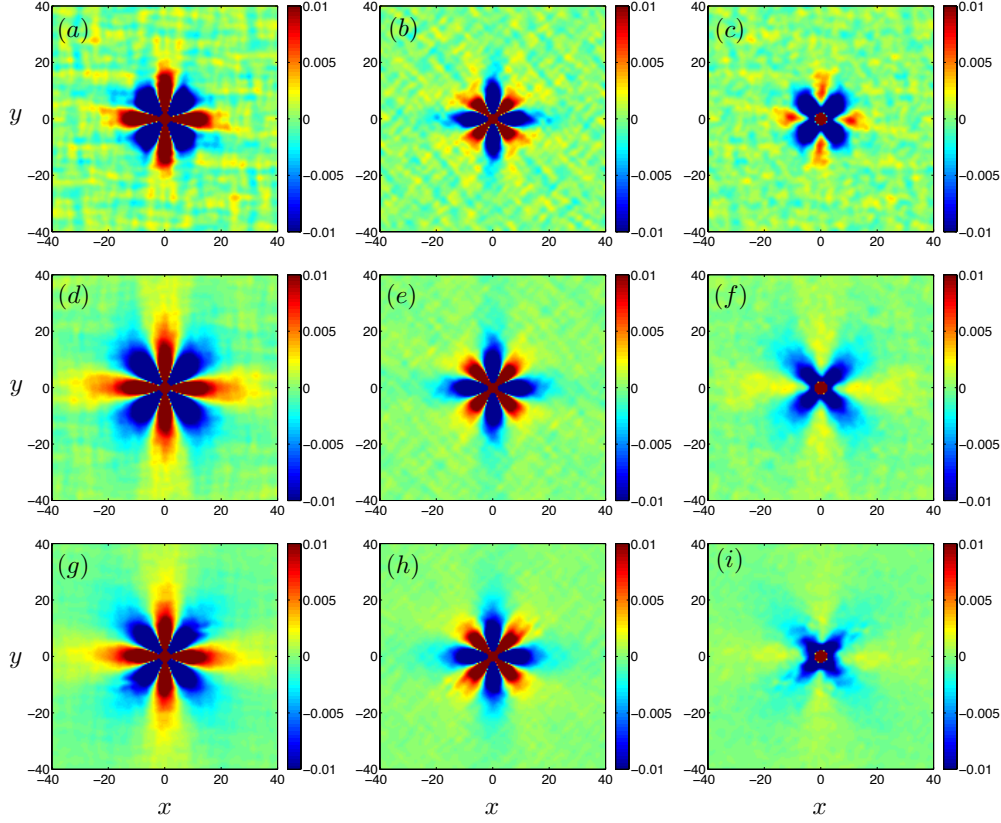
Figure 3.10: Spatial autocorrelation for $\dot{\epsilon}$, $\dot{\Psi}$ and $\dot{\omega}$ for 3 different shearing rate. From **left** to **right** : $C_{\dot{\epsilon}}/C_{\dot{\epsilon}}(r=0)$, $C_{\dot{\Psi}}/C_{\dot{\Psi}}(r=0)$, $C_{\dot{\omega}}/C_{\dot{\omega}}(r=0)$ and from **top** to **bottom** : $\dot{\gamma}=10^{-4}$, $\dot{\gamma}=10^{-5}$, $\dot{\gamma}=10^{-6}$.

In Fig. 3.11, we plot the power spectrum $S(\vec{k})$ for $\dot{\epsilon}$, $\dot{\Psi}$ and $\dot{\omega}$ for the same rates, $\dot{\gamma}=10^{-4},10^{-5},10^{-6}$. The quadrupolar symmetry in power spectrum of $\dot{\epsilon}$ and $\dot{\omega}$ fields indicates the emergence of slip lines along the vertical and horizontal directions. $S_{\dot{\Psi}}$ has less power along the maximum correlation directions $(\pi/4, 3\pi/4)$ compare to the $S_{\dot{\Psi}}$ along horizontal or vertical directions. We will discuss about the angular dependence of strain-rate fields in the next subsection.

35
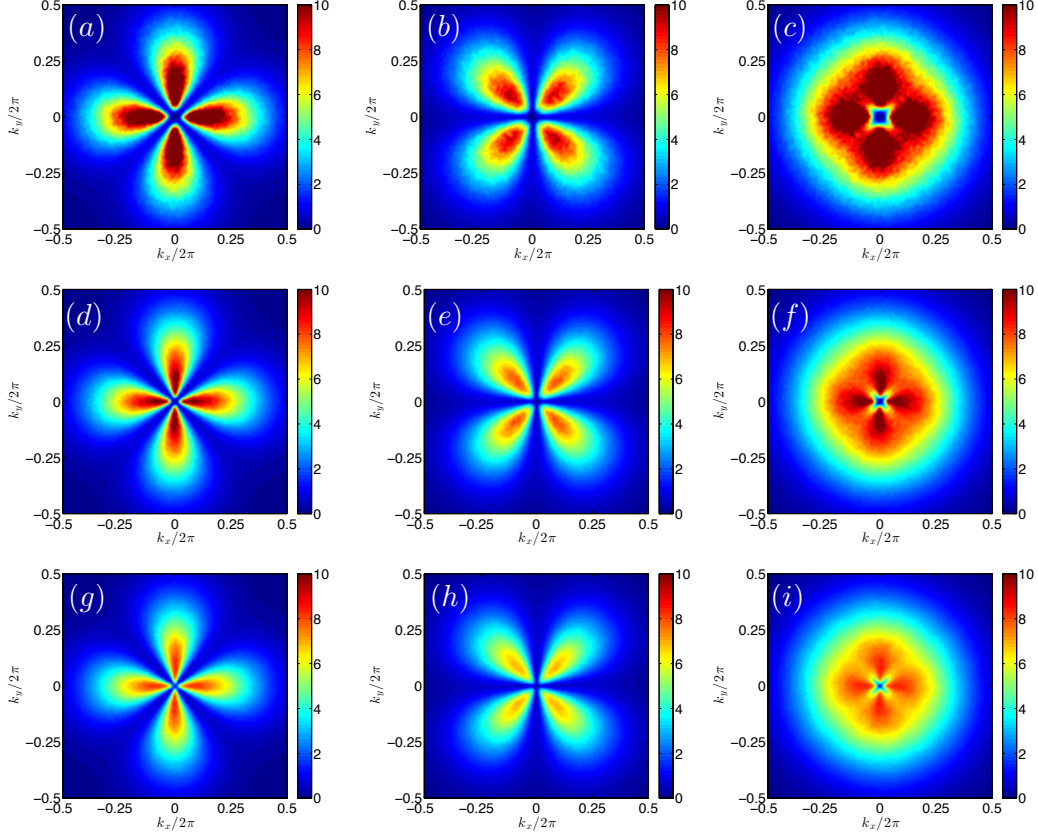
Figure 3.11: Power spectrum of $\dot{\epsilon}$, $\dot{\Psi}$ and $\dot{\omega}$ for 3 different shearing rate. From **left** to **right** : $S_{\dot{\epsilon}}$, $S_{\dot{\Psi}}$, $S_{\dot{\omega}}$ and from **top** to **bottom** : $\dot{\gamma} = 10^{-4}$, $\dot{\gamma} = 10^{-5}$, $\dot{\gamma} = 10^{-6}$.

Isotropic velocity field

In this part we are interested to study the shear strain-rate for various orientation. We can express shear strain-rate at an arbitrary angle θ as,

$$\dot{\tau}_T(\theta) = -\dot{\Psi}_{xy} \sin 2\theta + \dot{\epsilon}_{xy} \cos 2\theta \qquad (3.7)$$

In Fig. 3.12 we show the power spectrum for the shear strain rate, $\dot{\tau}_T$ for 3 orientation, $\theta = 0, \pi/8, \pi/4$ for an intermediate rate $\dot{\gamma} = 10^{-5}$. By construction,
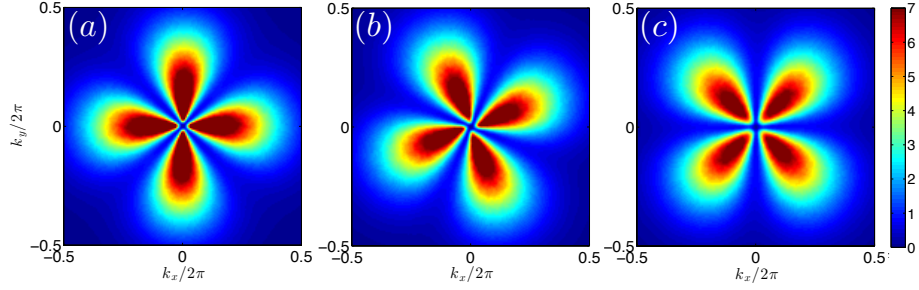
Figure 3.12: Power $S(k_x, k_y)$, for three different orientation of $\dot{\tau}_T(\theta)$: (a) $\theta = 0$, (b) $\theta = \pi/8$ and (c) $\theta = \pi/4$, for $\dot{\gamma} = 10^{-5}, L = 160$.

$\dot{\tau}(\theta = 0)$ and $\dot{\tau}_T(\theta = \pi/4)$ correspond to $\dot{\epsilon}$ and $-\dot{\Psi}$ respectively. Important point to note, although imposed shear along horizontal direction initiates deformation via the horizontal and vertical slip lines, the shear strain-rate power is almost angle invariant. This is a strong indication of the isotropic nature of the instantaneous velocity field.
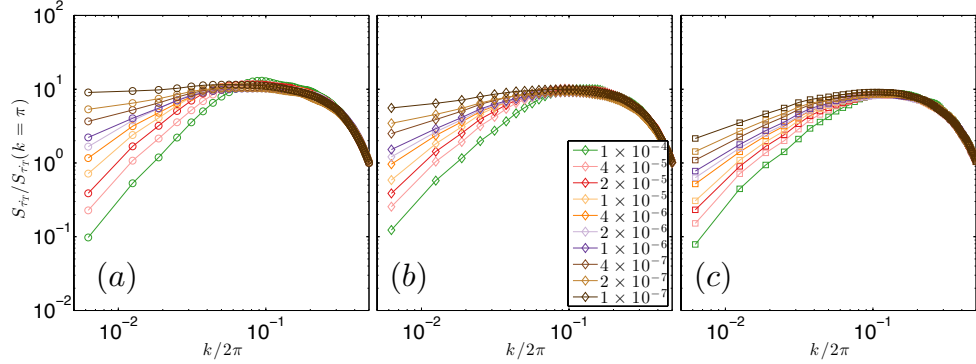
Figure 3.13: $S_{\dot{\tau}_T}/S_{\dot{\tau}_T}(k = \pi)$ vs. $k/2\pi$ where k is along θ for (a) $\theta = 0$, (b) $\theta = \pi/8$ and (c) $\theta = \pi/4$.

In Fig. 3.13, we plot the power along the maximum power direction for the three orientations of shear strain-rate, $\dot{\tau}_T$. For fast rates, we observe similar rate dependance of $\dot{\tau}_T(\theta)$ for different θ. The power of $\dot{\tau}_T(\theta)$ follows a flat spectrum for

intermediate k before it rolls off below $\xi k \approx 2\pi$. At vanishing rates, power of $\dot{\tau}_T$ approaches to an k independent regime at long wavelengths, which is a signature of power accumulated over several uncorrelated Eshelby flips. We believe for larger systems at low rates we would be able to converge to a θ-independent flat regime for $S_{\dot{\tau}_T}$.

To summarize, we have shown for the MD model, instantaneous velocity fields show long range spatial correlations. These correlations are of precisely the Eshelby form in the limit of low shearing rate. With increasing rate, the correlations are cut off to a certain length, ξ, below which it follows similar Eshelby behavior. It was also interesting to find that the shear strain-rate field is angle invariant indicating the isotropic nature of the velocity field.

Chapter 4

Finite Time Response

In this chapter we study the particle diffusion and the structure of associated long time plastic activities for MD. The diffusion coefficient is a measure of the accumulated correlations originated from the particle rearrangements. Here we also discuss about the connection between the rheology and diffusion constant for these sheared suspensions in the framework of an effective temperature and the correlation length.

4.1 Diffusive Behavior

4.1.1 Displacement Statistics

We first study the second moment of the displacement distribution. For this analysis we use the y-displacement, Δy of the individual particles, which are defined over a time during which a strain of amplitude, $\Delta\gamma = \dot{\gamma}\Delta t$, was applied. We do this for simplicity, as Δy is transverse to the flow direction and thus have no affine contribution from the horizontal shear flow. We would expect identical results for the x-displacements (Δx) once the appropriate background motion is subtracted off. To analyze the effect of elapsed strain on diffusion, we study the statistics of Δy on different strain interval of size $\Delta\gamma$.

In Figure 4.1a, we plot the mean squared displacement (MSD) over $\Delta\gamma$ vs. $\Delta\gamma$ for different rates, $\dot{\gamma} \in [1 \times 10^{-7}, 8 \times 10^{-3}]$ for $L = 40$. For fast rates, MSD has a sharp crossover from the *ballistic* behavior($\Delta y \propto \Delta\gamma$) at small $\Delta\gamma$ to *Diffusive* behavior($\Delta y^2 \propto \Delta\gamma$) at large $\Delta\gamma$. But irrespective of $\dot{\gamma}$, around $\Delta\gamma \approx 1$, $\langle\Delta y^2\rangle/2\Delta\gamma$ reaches a plateau value indicating the saturation of plastic activities in the system.

In Figure 4.1b, we show the non-Gaussian parameter, $\alpha = 3\langle\Delta y^2\rangle^2/\langle\Delta y^4\rangle$ for the y-displacement distributions. For a Gaussian like distribution, α should be unity. For relatively slower rates, Δy distributions appear to be non-Gaussian at small $\Delta\gamma$ and appear to reach the Fickian limit (both $\alpha = 1$ and $\langle\Delta y^2\rangle \propto \Delta\gamma$) at a much larger $\Delta\gamma \approx 1$. However, for fast rates Δy distributions are always Gaussian and crosses over to the Fickian limit at a similar $\Delta\gamma$.

(a) Scaled second moment   (b) Non-Gaussian parameter
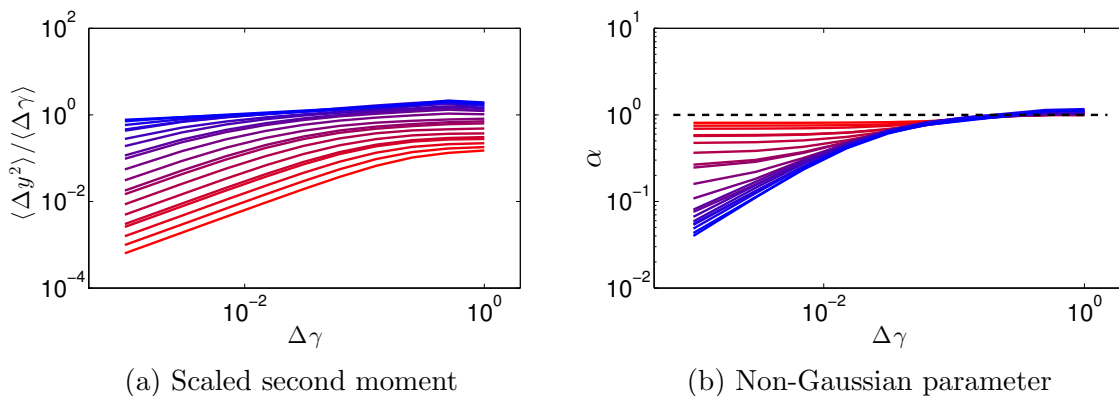
Figure 4.1: (a) $\langle\Delta y^2\rangle/\langle\Delta\gamma\rangle$ vs. $\Delta\gamma$ and (b) α vs. $\Delta\gamma$ for different rates, $\dot{\gamma}= [1, 2, 4, 8,$ $10, 20, 40, 80,$ $100, 200, 400, 800,$ $1000, 2000, 4000, 8000,$ $10000, 20000, 40000, 80000]$ $\times 10^{-7}$ for $L = 40$. Red correspond to a fast rate ($\dot{\gamma} = 8 \times 10^{-3}$) and blue correspond to a slow rate ($\dot{\gamma} = 1 \times 10^{-7}$). The bold dashed line in (b) corresponds to $\alpha = 1$.

Fig. 4.2 is a representative plot for the MSD for $L = 160$. In Fig. 4.3a, we plot the *Effective* diffusion constant, $D_e \doteq \lim_{\Delta\gamma\to\infty}\langle\Delta y^2\rangle/2\Delta\gamma$ vs. $\dot{\gamma}$ for three different system sizes, $L = 40, 80$ and 160. At large rates, D_e, is independent of L and follows a $\dot{\gamma}^{-1/3}$ power law with remarkable precision and for over four decades of rate for $L = 160$ system. At the lowest rates in the QS regime, a plateau is clearly visible for $L = 40$ and 80. In the inset, we plot D_e/L against $L\dot{\gamma}^{1/3}$. The data shows a good collapse, indicating that the QS diffusion, $D_{QS} \sim L$. This behavior has
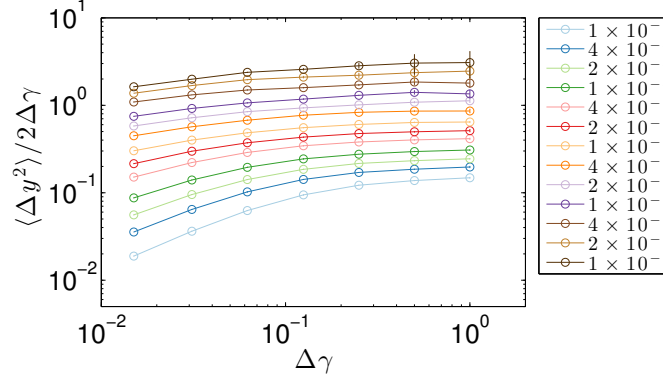
Figure 4.2: $\langle \Delta y^2 \rangle / 2\Delta\gamma$ vs. $\Delta\gamma$ for different $\dot{\gamma}$, $L = 160$.
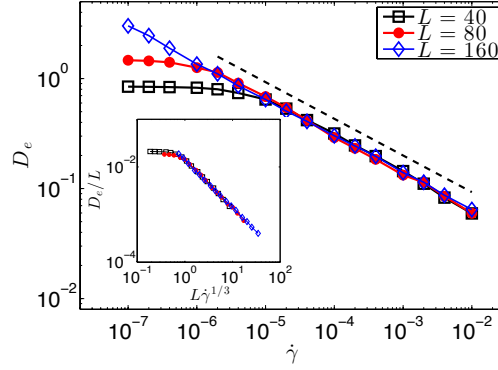
Figure 4.3: D_e vs. $\dot{\gamma}$ for $L = 40$, 80, and 160. The bold dashed line has a slope of $-1/3$. Inset: D_e/L vs. $L\dot{\gamma}^{1/3}$.

been understood to arise from system spanning lines of slip in molecular dynamics simulations of LJ glasses [84–87]. The bubble model exhibits these same slip lines in the QS regime. It is, rather, the rate dependence which is different here. Because of the relatively weak rate sensitivity, the $L = 160$ system shows a strongly rate dependent D_e even at $\dot{\gamma} = 10^{-7}$, as it has not yet reached its QS plateau.
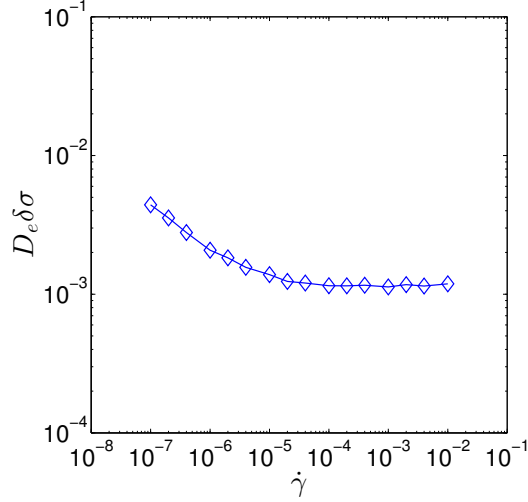
Figure 4.4: Effective athermal Stokes-Einstein temperature, $D_e \delta \sigma$, vs. $\dot{\gamma}$ for $\sigma_y = 0.0011$, $L = 160$.

4.1.2 Effective Temperature

Previously Ono *et. al.* [88, 89] have reported an *effective temperature*, T_{eff} for the sheared bubble system. They have defined T_{eff} as the fluctuations in the elastic energy and have shown it to scale with the product of the the diffusion constant, D and bulk viscosity, η. But all of their analysis were valid for very fast rates where the velocity distributions are Gaussian. Here in our system we are interested in much slower rates as well where the viscosity diverges due to the yield stress limit. We have already seen $\delta \sigma$ and D_e to follow power law like behavior with $\dot{\gamma}$. So instead of looking at $D\eta$ or $D_e \sigma$, we study $D_e \delta \sigma$. In Fig. 4.4 we plot $D_e \delta \sigma$ for the $L = 160$ system. $D_e \delta \sigma$ can be considered as an effective Stokes-Einstein temperature. Our results for $D_e \sigma$ agree with Ono *et. al.* [88, 89] for the $\dot{\gamma}$ where the studies overlap, but we show here that one can obtain a remarkably constant value of $D_e \delta \sigma$ for over

43

three decades in rate for the $L = 160$ system.

4.2   Finite Time Displacement

In this section, we study the spatial correlations and the evolution of the structure of non-affine displacement fields under shear. We first calculate the temporal auto-correlation of y-velocity, $C'_{v_y}(\Delta t)$ to get an idea of the characteristic strain windows to define displacement. C'_{v_y} is defined as,

$$C'_{v_y}(\Delta t) = \langle v_y(\vec{r}, t + \Delta t)v_y(\vec{r}, t)\rangle_{(\vec{r}, t)} \tag{4.1}$$

In Fig. 4.5, we plot $C'_{v_y}(\Delta t)$ normalized by the zero-time correlation, $C'_{v_y}(\Delta t = 0)$
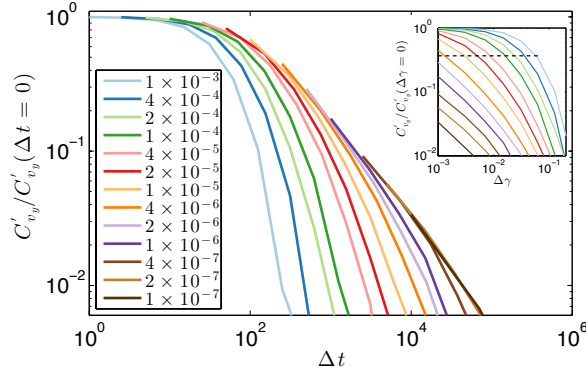
Figure 4.5: $C'_{v_y}(\Delta t)/C'_{v_y}(\Delta t = 0)$ for different $\dot{\gamma}$, $L = 160$.   Inset : $C'_{v_y}(\Delta \gamma)/C'_{v_y}(\Delta \gamma = 0)$ for same set of rates; bold dashed line correspond to $1/e$.

for the various rates. $C'_{v_y}(\Delta t)$ is strongly rate dependent. For faster rates C'_{v_y} decreases rapidly with time and crosses zero. On other hand at low $\dot{\gamma}$, C'_{v_y} decreases monotonically and takes longer in time to decorrelate compared to faster rates. But

from Fig. 4.2, we know that irrespective of $\dot{\gamma}$, we can obtain a diffusive regime based on the elapsed strain, $\Delta\gamma$. In inset of Fig. 4.5, we plot the temporal autocorrelation as a function $\Delta\gamma$. For $\dot{\gamma} \leq 10^{-4}$, normalized $C'_{v_y}(\Delta\gamma)$ decreases to $1/e$ times of the correlation at zero strain, around $\Delta\gamma^* \approx 10^{-2}$. This gives us a measure of a characteristic strain, $\Delta\gamma^*$ above which the velocities can be considered decorrelated for rates corresponding to $\dot{\gamma} \leq 10^{-4}$. Fig. 4.6 shows typical map of the x-displacement, u_x in left (Fig. 4.6a) and y-displacement, u_y in right (Fig. 4.6b), for $\Delta\gamma^*$, occurred between strain of 125% and 126% for $\dot{\gamma} = 10^{-5}$. Black means the particles moved horizontally towards left in Fig. 4.6a and vertically downward in Fig. 4.6b. We can observe long slip lines at $\dot{\gamma} = 10^{-5}$ but those are not system spanning as one expect in QS limit.
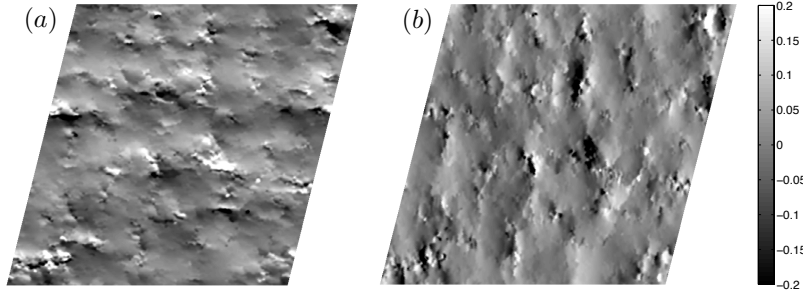
Figure 4.6: Typical real space map for displacements defined over $\Delta\gamma = 1\%$ for $\dot{\gamma} = 10^{-5}$: (a)u_x, (b)u_y

4.2.1 Correlation Length, $\xi \propto \dot{\gamma}^{-1/3}$

Next we look into the spatial correlation of the displacement field, similar to the velocity field [Sec. 3.2.2]. We calculate the spatial autocorrelation of y-displacement

(defined over certain $\Delta\gamma$)[1],

$$C_{u_y}(\vec{R}) = \langle u_y(\vec{R} + \vec{r}, t)u_y(\vec{r}, t)\rangle_{(\vec{r},t)} \tag{4.2}$$
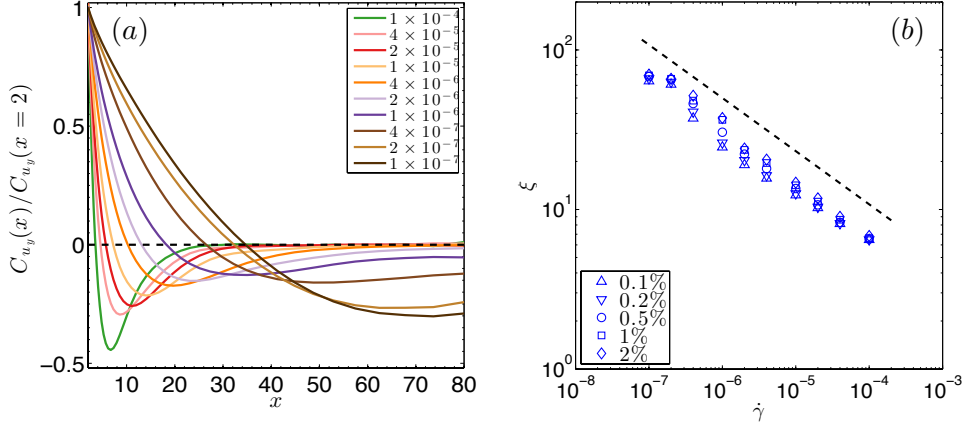
Figure 4.7: (a) $C_{u_y}(R = x)/C_{u_y}(x = 2)$ for different $\dot{\gamma}$, $L = 160$ where u_y is defined over $\Delta\gamma^*$; bold dashed line shows zero correlation. (b) ξ vs. $\dot{\gamma}$ for different $\Delta\gamma$; bold dashed line has a slope of $-1/3$.

In Fig. 4.7a, we plot C_{u_y}, along the x-separations, normalized by the $x = 2$ values, for various shearing rates, $\dot{\gamma} \leq 10^{-4}$ where u_y is defined for a strain of $\Delta\gamma^*$. The curves suggest that C_{u_y} is very sensitive to $\dot{\gamma}$. At $\dot{\gamma} = 10^{-4}$, C_{u_y} has a sharp dip and an unique minimum at around 6 particle distance before approaching to zero correlation at bigger distance. With decreasing $\dot{\gamma}$, not only the location of the minimum increases suggesting a growing correlation length, the structure of the correlation curves have noticeable changes. For $\dot{\gamma} \leq 10^{-6}$, the correlation does not converge to zero correlation at larger lengths, which can be thought as an artifact of the finite system size. Then we study the correlation of y-displacements defined over

---

[1]Details of displacement calculation can be found in Appendix. A

various $\Delta\gamma$. In Fig. 4.7b, we plot the location, ξ, of the minima of each C_{u_y} curve as a function of rate for 5 different $\Delta\gamma$. We observe for $10^{-6} < \dot{\gamma} \leq 10^{-4}$, the data can be well described by a $\xi \sim \dot{\gamma}^{-1/3}$ for every set of $\Delta\gamma$. As we decrease the rate and go beyond, $\dot{\gamma} \leq 10^{-6}$, the correlation lengths tend to saturate at the system size and ξ departs from the $\dot{\gamma}^{-1/3}$ scaling regime.
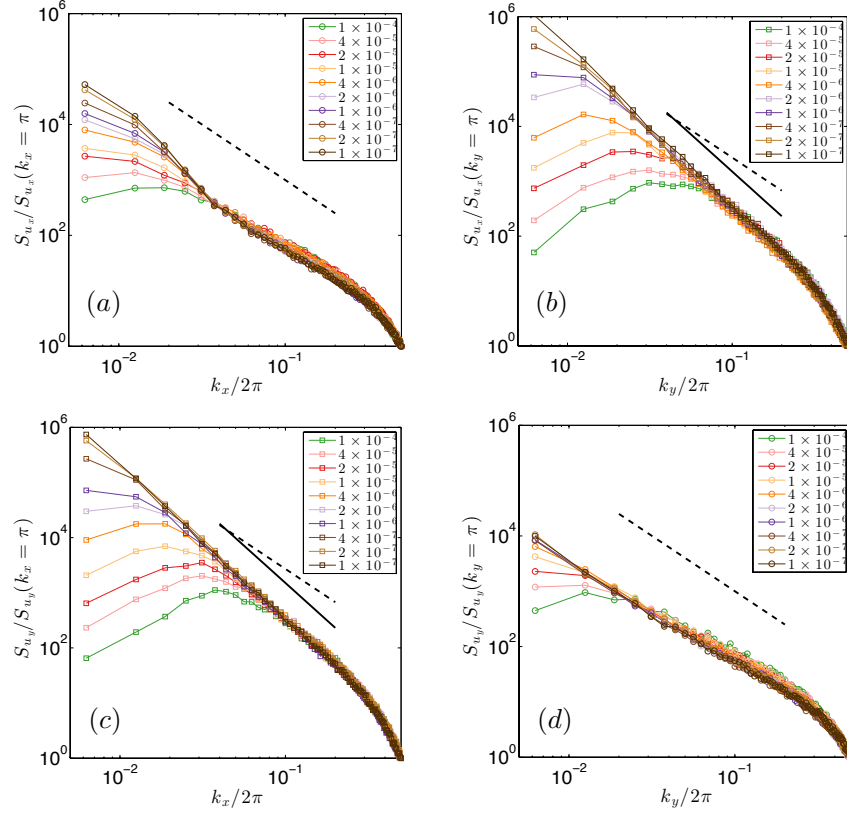
Figure 4.8: (a) S_{u_x} along k_x, (b) S_{u_x} along k_y, (c) S_{u_y} along k_x and (d) S_{u_y} along k_y for different strain rates. The bold dashed lines have slopes of -2 and bold solid lines (in (b) and (c)) have slopes of -2.7.

In Fig. 4.8a and 4.8b, we plot the power of x-displacements (defined overr $\Delta\gamma = 1\%$) along longitudinal (k_x) and transverse (k_y) direction respectively for various

rates. In Fig. 4.8c and 4.8d, we plot the power of y-displacements (defined over $\Delta\gamma = 1\%$) along transverse (k_x) and longitudinal (k_y) direction respectively for different rates. Similar to Fig. 3.7b and 3.7c, we observe a development of peak in Fig. 4.8b and Fig. 4.8c, whose location shifts to increasing k with increasing $\dot{\gamma}$. The transverse power for displacements show a much stronger $k-$dependance than the transverse power for instantaneous velocities following $k^{-2.7}$ instead of k^{-2}. The abrupt rise in the longitudinal power for u_x at long wavelength (in Fig. 4.8a) can be understood as the artifact of finite size effect due to Lees Edwards boundary condition.
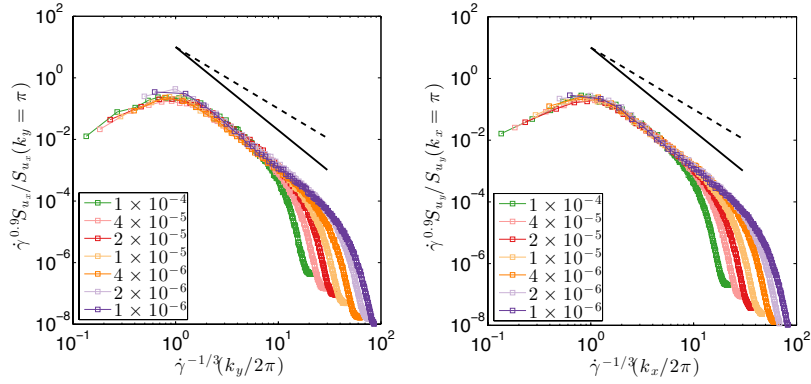
Figure 4.9: Left: Normalized S_{u_x} along cuts of k_y scaled by $\dot{\gamma}^{1/3}$, Right: Normalized S_{u_y} along cuts of k_x scaled by $\dot{\gamma}^{1/3}$. The bold dashed lines and solid lines have slopes of -2 and -2.7 respectively.

In Fig. 4.9, we show the displacement powers along transverse direction (as in Fig. 4.8b and 4.8c) scaled by $\dot{\gamma}^{(2.7/3)}$ vs $\dot{\gamma}^{-1/3}(k/2\pi)$. We observe a remarkable collapse of the data for two decades of rates. This agrees with the $\dot{\gamma}$ behavior of correlation length, $\xi \sim \dot{\gamma}^{-1/3}$ for $10^{-6} < \dot{\gamma} \leq 10^{-4}$ measured in real space for $\Delta\gamma = 1\%$ (in Fig. 4.7b). The increase of power with increasing k at long wavelength (corresponding

to lengths bigger than ξ) is due to the wavelength dependent damping nature of the displacement field in MD dissipation mechanism.

4.2.2 Relation between ξ and D_e

Now the big question is whether there is a connection between the correlation length, ξ and the diffusion coefficient, D_e. In 2009, Lemaitre *et. al.* [84] gave an argument that the effective diffusion constant is related to a characteristic length, l, as, $D_e \sim l \ln(L/l)$. In this thesis we show that the correlation length follows $\xi \sim \dot{\gamma}^{-1/3}$. ξ can be thought as the average length of the slip lines, which are particularly oriented along the maximal shear direction. If we imagine that the system is accommodating the strain we are injecting by organizing in these slip lines that are uncorrelated in space, then following [84], we can explain the rate dependence of D_e as, $D_e \sim \xi \sim \dot{\gamma}^{-1/3}$.
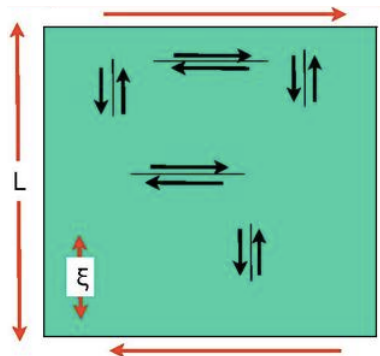
Figure 4.10: Slip lines of length ξ are primarily aligned along the horizontal and vertical directions.

4.2.3 Structure of Displacement Field

Here we present a detailed analysis of the structure of the displacement field and how it changes when the rate is varied or defined over a different strain window. To this purpose, we focus on cartesian components of the displacement gradients[2]. The strain tensor in two dimension can be expressed as,

$$\nabla u = \begin{bmatrix} \partial_x u_x & \partial_y u_x \\ \partial_x u_y & \partial_y u_y \end{bmatrix} \qquad (4.3)$$

In Fig. 4.11, we study the dependance of strain interval, $\Delta\gamma$ on 3 different measures of strain, $\epsilon = (\partial_x u_y + \partial_y u_x)/2$, $\Psi = (\partial_x u_x - \partial_y u_y)/2$ and $\omega = (\partial_y u_x - \partial_x u_y)/2$ for $\dot\gamma = 10^{-5}$. We plot typical strain maps normalized by their respective Root Mean Square (RMS) values for $\Delta\gamma = 0.1\%, 0.2\%, 0.5\%, 1\%, 2\%$. As we go from top to down, we increase our strain interval and as we proceed from left to right we present the ϵ, Ψ and ω field respectively in order. At $\Delta\gamma = 0.1\%$, the strain maps of ϵ, Ψ and ω appears to be strikingly similar to their instantaneous counterparts of $\dot\epsilon$, $\dot\Psi$ and $\dot\omega$ (Fig. 3.9d, 3.9e, 3.9f). With increasing $\Delta\gamma$, ϵ and ω field become more anisotropic. For large strain intervals, $\Delta\gamma \geq 1\%$, we can observe elongated vertically oriented slip lines with counter-clockwise vorticity as white lines in ϵ maps and black lines in ω maps. Similarly long horizontally oriented slip lines with clockwise vorticity appear as white lines in both ϵ and ω maps. Ψ fields look to be relatively insensitive to the choice of various $\Delta\gamma$.

In Fig. 4.12, we plot the time averaged spatial auto correlation function for ϵ,

---

[2]See Appendix. B for gradient calculations on sheared systems

Ψ and ω for various $\Delta\gamma$ for $\dot{\gamma} = 10^{-5}$. C_ϵ shows four fold symmetry with strong correlations along the maximal shear directions, $\theta = 0$ and $\theta = \pi/2$. With increasing $\Delta\gamma$, the correlation grows but eventually starts to saturate over $\Delta\gamma \geq 1\%$. C_ψ is relatively insensitive to $\Delta\gamma$ variation. C_ω shows increasing anisotropy with increasing $\Delta\gamma$ with growing positive correlations along the maximal shear directions. Asymmetry in ω correlations along x and y-direction, visible for $\Delta\gamma = 2\%$, is an artifact of averaging over many different Lees-Edwards cell.

In Fig. 4.13, we plot the power spectrum, $S(\vec{k})$ for ϵ, Ψ and ω for various $\Delta\gamma$ for $\dot{\gamma} = 10^{-5}$. Both ϵ and Ψ powers have prominent quadrupolar symmetry, similar to the real space correlation irrespective of $\Delta\gamma$. With increasing $\Delta\gamma$, ω field becomes more anisotropic, which is visible in the right column of Fig. 4.13, as we go down from top to bottom.

Fig. 4.14a shows the power of ϵ, along k_x for $k_y = 0$ and Fig. 4.14b shows power of Ψ along $k_x = k_y$ direction in a log-log scale for various $\Delta\gamma$, $\dot{\gamma} = 10^{-5}$. Overall powers are normalized by the respective power at an wavelength of 2 particle distance. S_Ψ is relatively flat for various $\Delta\gamma$, before rolling off to zero at infinite wavelength. S_ϵ depends on $\Delta\gamma$ as the length of slip line grows with increasing amount of strain. With increasing $\Delta\gamma$, there is a development of peak at low k for S_ϵ before decaying at high k in a power law manner. The location of the peak in $\Delta\gamma$ independent and agrees with the observation of similar correlation length for different $\Delta\gamma$ (in 4.7b). The exponent for the power law increases (in negative scale) from zero at $\Delta\gamma = 0.1\%$ to 0.7 at $\Delta\gamma = 1\%$. It is believed that at diffusive limit for QS system, the system will be saturated with system spanning slip lines and the power law exponent should

become constant, i.e., invariant of $\Delta\gamma$.

Anisotropic Displacement Field

In Sec. 3.2.3 we have seen the velocity field is isotropic for various rates. Here we want to examine the characteristics of the long time displacement field. We look at the component of the shear strain at different orientation. Shear strain at an arbitrary angle θ can be expressed as,

$$\tau_T(\theta) = -\Psi_{xy} \sin 2\theta + \epsilon_{xy} \cos 2\theta \qquad (4.4)$$

By construction, $\tau(\theta = 0)$ and $\tau_T(\theta = \pi/4)$ correspond to ϵ and $-\Psi$ respectively.

In Fig. 4.15 we show the power spectrum for the τ_T for 3 orientation, $\theta = 0, \pi/8, \pi/4$ for $\Delta\gamma = 1\%$, $\dot{\gamma} = 10^{-5}$. We observe more power along the principal shear directions for $\theta = 0$ than $\theta = \pi/8$ and $\theta = \pi/4$. This indicates the anisotropic nature of the displacement field. It can be understood by the preference of the slip lines to organize along the maximal shear directions (horizontal and vertical) for a simple shear geometry.

In Fig. 4.16, we plot the power along the maximum power direction for the three orientations of shear strain, τ_T. S_{τ_T} has a stronger k-dependence, $S \sim k^{-0.7}$ for $\theta = 0$ than $\theta = \pi/8, \pi/4$. With increasing rates the power starts to roll off from the master curve at higher k, suggesting a decreasing correlation length. In inset of Fig. 4.16a and Fig. 4.16c, we observe that for intermediate rates, $10^{-5} \leq \dot{\gamma} \leq 4 \times 10^{-5}$, the data collapses when we scale them by the appropriate power, which signifies $\xi \sim \dot{\gamma}^{-1/3}$.

In summary, we have shown that long time particle diffusion is connected to the

rheology via an effective Stokes-Einstein temperature. The rate dependence of D_e can be explained by the similar behavior of correlation length of the displacement fields. This correlation length scales the same way with rate as the correlation length extracted from the instantaneous response. We have also showed that the finite time displacement fields become increasingly anisotropic at long strain intervals. The correlations along the primary shear directions are stronger than any other orientation of the shear strain.
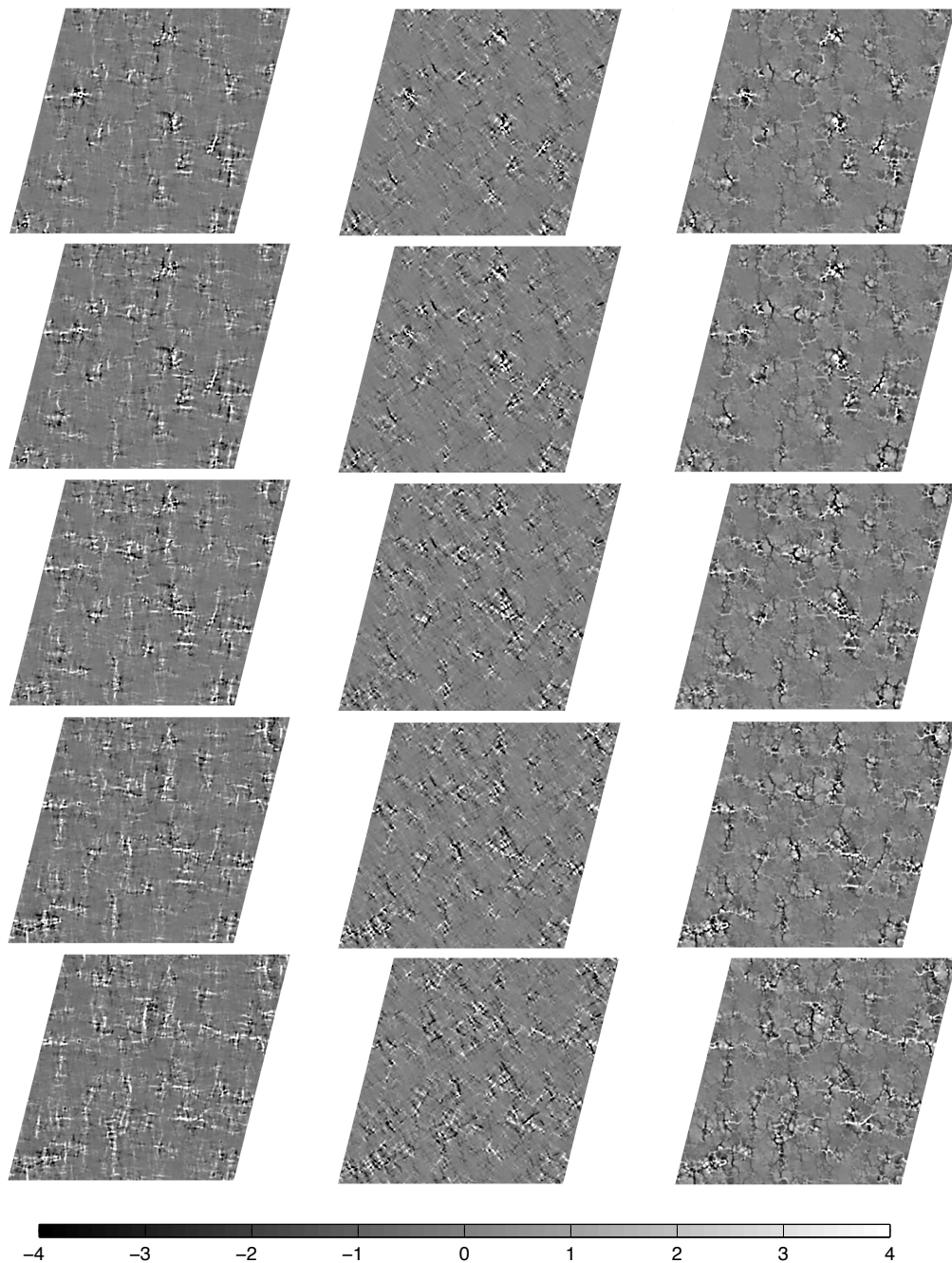
Figure 4.11: Typical maps of ϵ, Ψ and ω for 5 different strain windows for $\dot{\gamma} = 10^{-5}$. From **left** to **right** : ϵ/ϵ_{RMS}, Ψ/Ψ_{RMS}, ω/ω_{RMS} and from **top** to **bottom** : $\Delta\gamma = 0.1\%$, $\Delta\gamma = 0.2\%$, $\Delta\gamma = 0.5\%$, $\Delta\gamma = 1\%$, $\Delta\gamma = 2\%$.
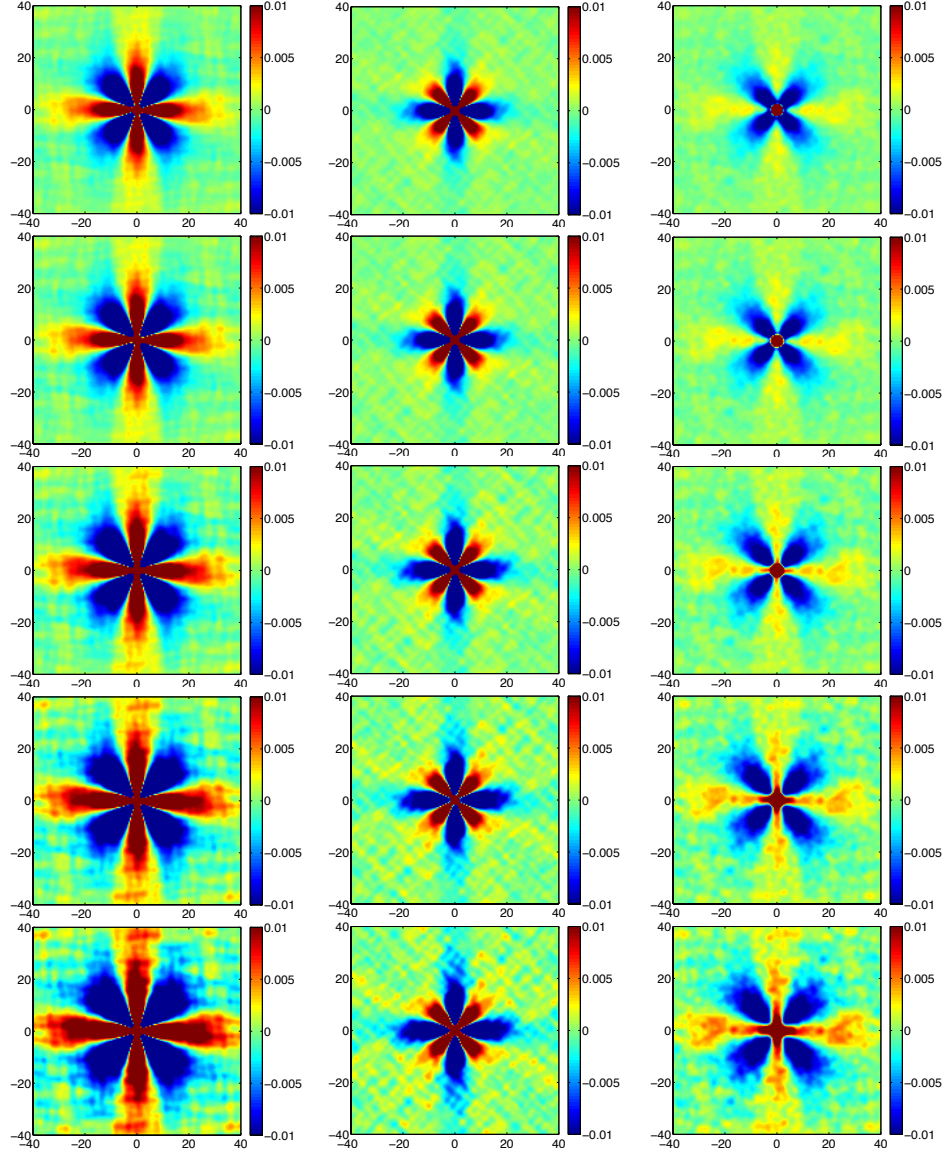
Figure 4.12: Spatial autocorrelation of ϵ, Ψ and ω for 5 different strain windows for $\dot{\gamma} = 10^{-5}$. From **left** to **right** : $C_\epsilon/C_\epsilon(r=0)$, $C_\Psi/C_\Psi(r=0)$, $C_\omega/C_\omega(r=0)$ and from **top** to **bottom** : $\Delta\gamma = 0.1\%$, $\Delta\gamma = 0.2\%$, $\Delta\gamma = 0.5\%$, $\Delta\gamma = 1\%$, $\Delta\gamma = 2\%$.
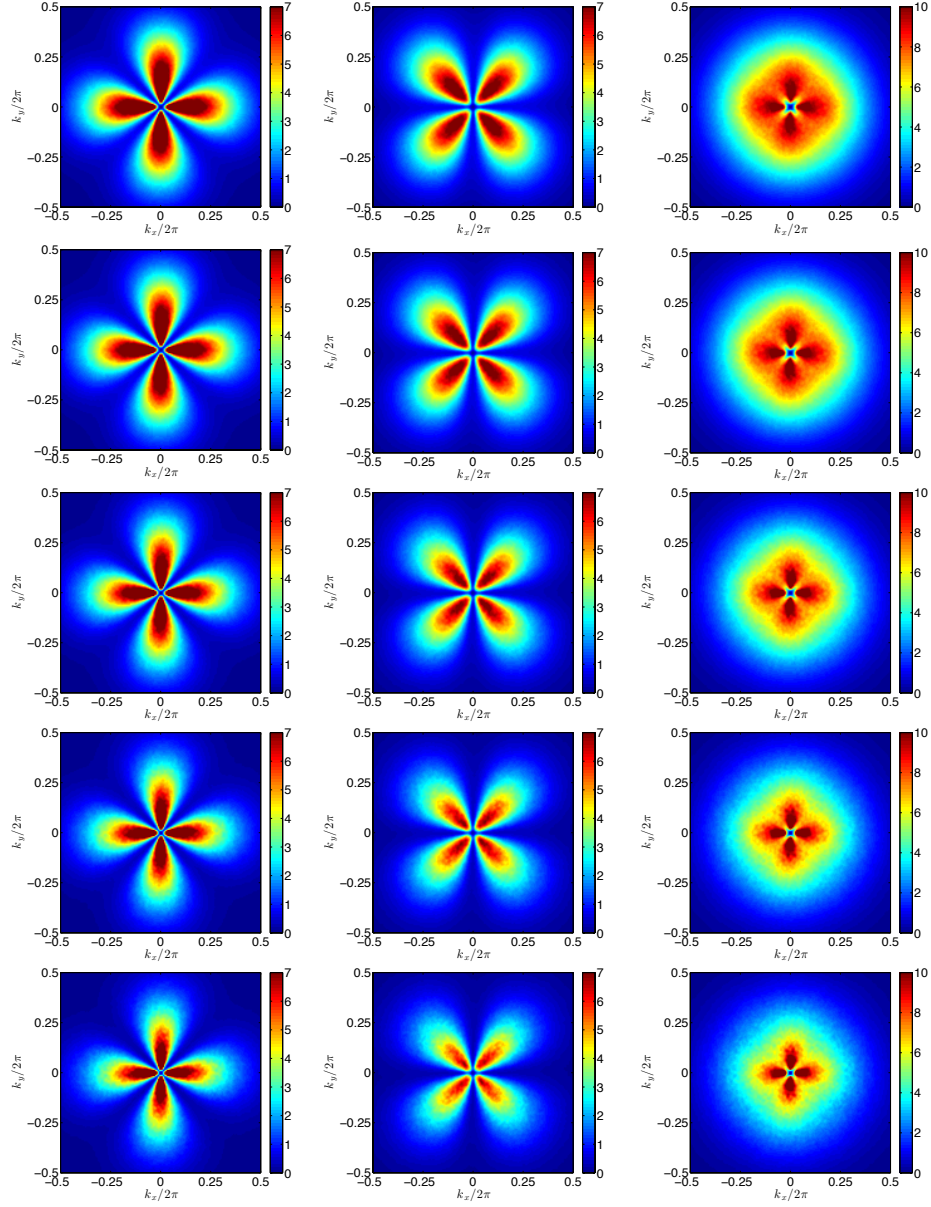
Figure 4.13: Power spectrum of ϵ, Ψ and ω for 5 different strain windows for $\dot{\gamma} = 10^{-5}$. From **left** to **right** : S_ϵ, S_Ψ, S_ω and from **top** to **bottom** : $\Delta\gamma = 0.1\%$, $\Delta\gamma = 0.2\%$, $\Delta\gamma = 0.5\%$, $\Delta\gamma = 1\%$, $\Delta\gamma = 2\%$.

Figure 4.14: (a) $S_\epsilon/S_\epsilon(k = \pi)$ along $\theta = 0$ for 5 different strain interval. (b) $S_\Psi/S_\Psi(k = \pi)$ along $\theta = \pi/4$ for the same strain intervals, for $\dot{\gamma} = 10^{-5}, L = 160$.
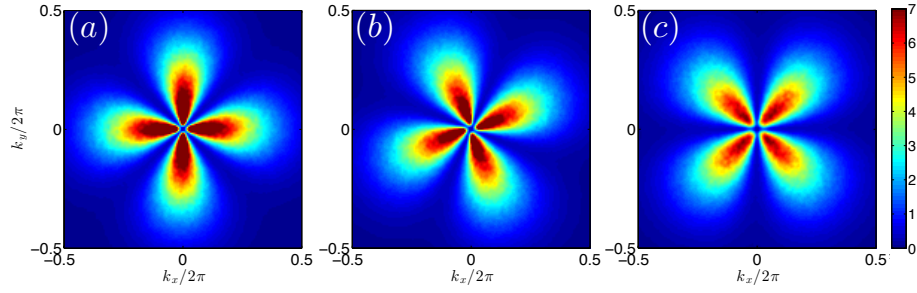
Figure 4.15: Power $S(k_x, k_y)$, for three different orientation of the shear-strain tensor, $\tau_T(\theta)$: (a) $\theta = 0$, (b) $\theta = \pi/8$ and (c) $\theta = \pi/4$, for $\dot{\gamma} = 10^{-5}, \Delta\gamma = 10^{-5}, L = 160$.

57
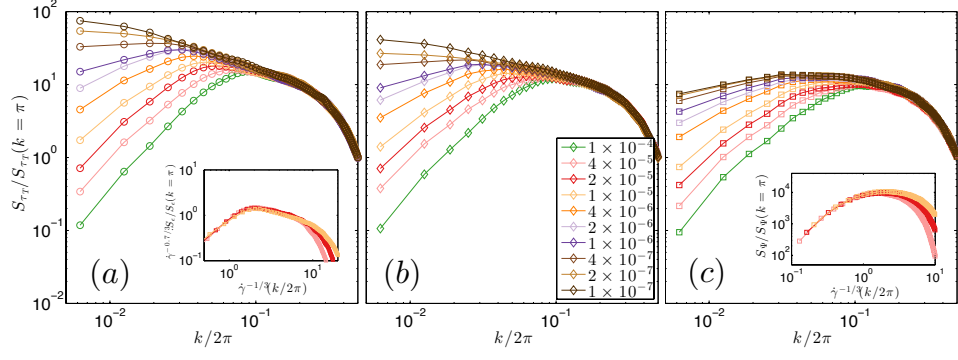
Figure 4.16: $S_{\tau_T}/S_{\tau_T}(k = \pi)$ vs. $k/2\pi$ where k is along θ for (a) $\theta = 0$, (b) $\theta = \pi/8$ and (c) $\theta = \pi/4$, for $\Delta\gamma = 1\%$. By construction, $S_{\tau_T}(\theta = 0) = S_\epsilon$ and $S_{\tau_T}(\theta = \pi/4) = S_\Psi$. Inset of (a): $\dot{\gamma}^{-0.7/3}S_\epsilon/S_\epsilon(k = \pi)$ vs. $\dot{\gamma}^{-1/3}k/2\pi$ for 3 rates, $\dot{\gamma} = 10^{-5}, 2 \times 10^{-5}, 4 \times 10^{-5}$. Inset of (c): $S_\Psi/S_\Psi(k = \pi)$ vs. $\dot{\gamma}^{-1/3}k/2\pi$ for same rates as in Inset(a) $\dot{\gamma} = 10^{-5}, 2 \times 10^{-5}, 4 \times 10^{-5}$.

Chapter 5

Pair Drag

In the previous chapters we have discussed the connection between the rheology and particle diffusion of sheared suspensions using the simple MD version of the Durian's bubble model [1]. We have seen that a single correlation length can be obtained from the spatial structure which explains the diffusive behavior and the rheology in the range of rates where effective temperature is almost constant. In this chapter we study the PD version of the bubble model, to examine our hypothesis of correlation length and effective temperature as the connection between macroscopic flow stress and microscopic particle diffusion.

5.1 Rheology and Diffusion
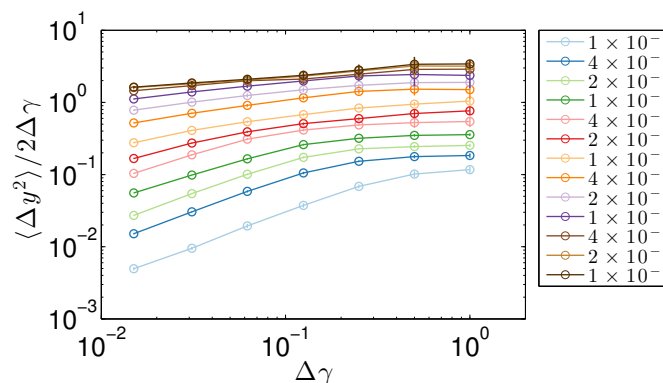
Figure 5.1: $\langle \Delta y^2 \rangle / 2\Delta\gamma$ vs. $\Delta\gamma$ for different rates, $L = 160$ for PD.

In Fig. 5.1, we plot the MSD over elapsed strain, $\Delta\gamma$ for different $\dot{\gamma}$. We observe similar behavior as the Mean Drag version, depicting diffusive motion above long strain intervals, $\dot{\gamma} \approx 1$. For fast rate, $\dot{\gamma} = 10^{-1}$, we can see a clear distinction between *ballistic* and *diffusive* behavior as we increase $\Delta\gamma$.

Next we present the rheology and diffusion data over 4 decades of shearing rates. In

Fig. 5.2a, we show flow stress, σ for $L = 160$. At low rates σ approaches to an yield stress and with increasing $\dot{\gamma}$, σ increases following a HB equation $\sigma - \sigma_y \sim \dot{\gamma}^{1/2}$. The exponent of the HB form is very different in this version of drag mechanism that what we observe in the MD variant. The $\dot{\gamma}^{1/2}$ behavior of PD is reminiscent of the experimental observations in microgel paste and dense emulsions [7, 8] and agrees with previous results using PD [3]. In Fig. 5.2b, we plot the effective diffusion constant, D_e vs. $\dot{\gamma}$ for $L = 160$. At low rates $\dot{\gamma} \leq 10^{-4}$, D_e starts to plateau showing saturation of spatial correlation at system size. For faster rates $\dot{\gamma} > 10^{-4}$, D_e follows a power law, $D_e \sim \dot{\gamma}^{-1/2}$. In the inset of Fig. 5.2b, we show the measure for effective temperature $D_e \delta\sigma$, similar to MD case, which has a very little variation over 4 decades of rate.

(a) σ vs. $\dot{\gamma}$ (b) D_e vs. $\dot{\gamma}$
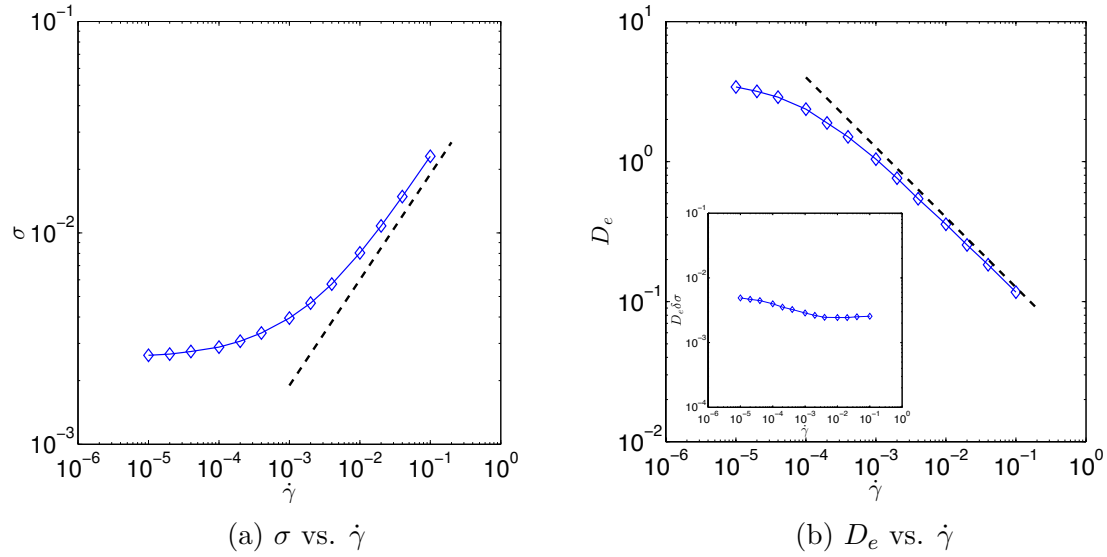
Figure 5.2: (a) Flow curve, σ vs. $\dot{\gamma}$ for PD, $L = 160$. The bold black dashed line has a slope of 1/2. (b) D_e vs. $\dot{\gamma}$ for the PD, $L = 160$. The bold black dashed line has a slope of -1/2. Inset: Effective athermal Stokes-Einstein temperature, $D_e \delta\sigma$ for $\sigma_y = 0.0012$.

5.2 Finite Time Plastic Correlation

Following Sec. 4.2, we study the finite time displacement correlation in this section for the PD dissipation mechanism. We focus on the correlation of u_y along x-axis (transverse direction).
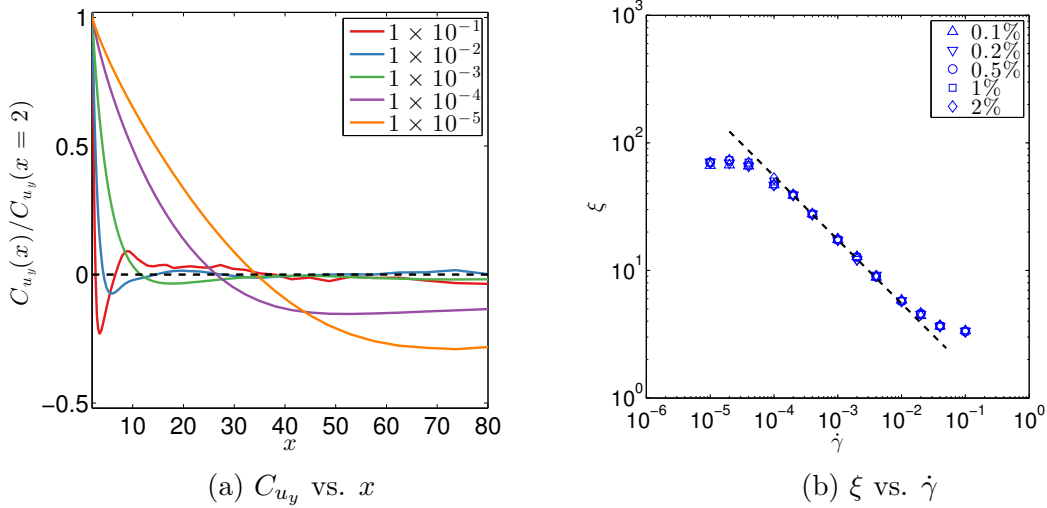
Figure 5.3: (a) $C_{u_y}(R = x)/C_{u_y}(x = 2)$ for the PD model for different $\dot{\gamma}$ and a particular $\Delta\gamma = 1\%$. The bold dashed line shows zero correlation. (b) ξ vs. $\dot{\gamma}$ for 5 different $\Delta\gamma$. The bold dashed line has a slope of -1/2.

In Fig. 5.3a, we plot correlation of u_y separated along the x-separations, normalized by the $x = 2$ values, for various shearing rates, where u_y is defined over a strain of 1%. Then we take the first minimum of the C_{u_y} curves for different $\dot{\gamma}$. In Fig. 5.3b, we also include data for 5 different $\Delta\gamma$ to define the displacements. We observe for all $\Delta\gamma$, the correlation length, ξ follows $\xi \sim \dot{\gamma}^{-1/2}$ for intermediate rates. At low rates ($\dot{\gamma} < 10^{-4}$), ξ plateau to a rate independent value suggesting the saturation of spatial correlation. At very high rate ($\dot{\gamma} > 10^{-2}$) the correlation decreases to particle

scale which is evident from the departing of ξ from the power law to a constant value of 3 particle diameter. We verify the $\dot{\gamma}^{1/2}$ dependence of ξ by looking at the transverse power of u_y. In Fig. 5.4a, we plot S_{u_y} along the transverse direction, k_x for various rates. In Fig. 5.4b, we show the same data scaled by appropriate power of $\dot{\gamma}$ against $k_x/2\pi$ normalized by $\dot{\gamma}^{1/2}$. We observe a remarkable data collapse over 2 decades of rate, $10^{-4} \leq \dot{\gamma} \leq 10^{-2}$. For wavelengths corresponding to $\lambda \leq \xi$, the transverse power shows a power law with an exponent of -2.7, similar to what was observed in the MD case. At long wavelength limit, displacement power is flat. This can be understood by the fact that in PD, all modes are equally damped regardless of wavevector.

(a) S_{u_y} vs. k_x (b) Normalized S_{u_y} vs. k_x
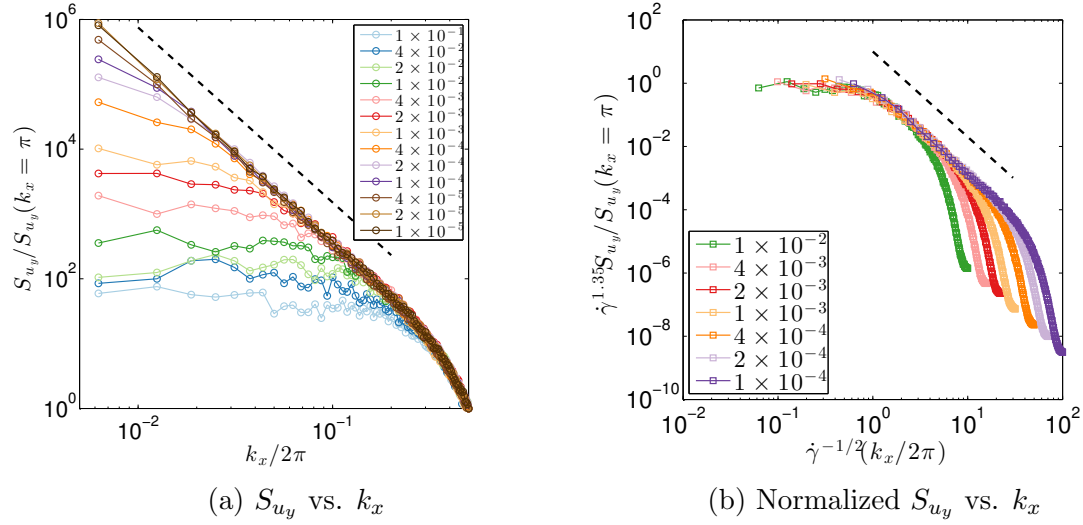
Figure 5.4: (a) S_{u_y} along cuts of k_x. (b) Normalized S_{u_y} along cuts of k_x scaled by $\dot{\gamma}^{1/2}$ for rates, $\dot{\gamma} \in [10^{-4}, 10^{-2}]$. The bold dashed lines have slopes of -2.7.

63

Chapter 6

Summary and Conclusion

We performed numerical simulations to study the behavior of soft particle jammed suspensions under simple shear. We used Durian's bubble model [1] where the repulsive forces due to the contact deformation of the soft particles are balanced by the viscous forces caused by the surrounding fluid flow. The model shows yield stress behavior following a Herschel-Bulkley power law [2], $\delta\sigma = \sigma - \sigma_y \sim \dot{\gamma}^{\beta}$ at finite rates. β is roughly 1/3 for the mean drag version of the model where viscous forces arise in response to the motion of the particle with respect to the background fluid flow – appropriate for situations where the dominant effects are due to the motion of fluid away from the particles such as particles moving at an air-water interface in a bubble raft [5, 6, 20]. β is roughly 1/2 for the pair drag version of the model where viscous forces arise in response to the motion of the particle with respect to its immediate neighbors – appropriate for situations where the dominant effects are due to the shear in the lubricating fluid films between particles [3,7,8]. Both of these models are in agreement with the respective experiments where interfacial or bulk drag would be expected to dominate.

The dissipated energy and velocity distributions are Gaussian at high rate but very non-Gaussian at low rates. This is consistent with the emergence of bursty, intermittent behavior as seen in other athermal, driven systems [27]. In the smallest samples at the lowest rates, we can detect a bonafide QS regime where a peak at low dissipation rate in the dissipation rate distribution corresponds to the times when the system is not experiencing any significant plasticity, and the location of this QS peak scales with rate accordingly.

We also studied single particle displacement statistics. At the highest rates,

these show a sharp crossover from ballistic to diffusive behavior at a strain of the order of unity. In this regime the displacement distributions are essentially Gaussian at all times (with a very small kurtosis), from the ballistic through the diffusive regimes resembling what one might observe in an ideal gas with a characteristic collision time of the order of unity. In contrast, at low rates, the displacement distributions are strongly non-Gaussian at short times. In the QS regime, the kurtosis of the displacement has a similar power-law dependence on time as QS simulations of conventional Lennard-Jones glasses.

The long time effective diffusion coefficient (D_e) saturates at a rate independent value in the QS regime. This QS value of D_e scales linearly with the length of the system, also in agreement with previous results on conventional Lennard-Jones glasses. With increasing rate, De decreases following a power law, $D_e \sim \dot{\gamma}^{-1/3}$ for mean drag version. Again, in analogy with conventional LJ simulations, one would expect this decrease in D_e to be controlled by a corresponding decreasing correlation length in the displacement fields.

Irrespective of the drag mechanism, there is an effective Stokes-Einstein temperature, T_{eff}, which remains constant over many orders of magnitude in shear rate. The constancy of this effective temperature can explain the connection between rheology and diffusion. Our results agree with Ono *et. al.* [89] for $D_e\sigma$, but we find it interesting that $D_e\delta\sigma$ remains constant over a much broader range of shearing rates than $D_e\sigma$, and we suspect that $D_e\delta\sigma$ gives a better measure of the effective temperature in the QS regime.

For mean drag dissipation, we studied the spatial correlations of instantaneous

velocity and finite time displacement fields to quantify the spatial correlations in plastic rearrangements. We measured a correlation length (ξ) which follows $\xi \sim \dot{\gamma}^{-1/3}$ for intermediate rates. At low rate, ξ saturates near the system size analogously to D_e. In analogy with conventional molecular dynamics simulations of LJ glasses, we expected to see this growing length in the displacement fields along with the growing value of D_e. However, we were surprised to see the same length here in the velocity fields. The velocity correlations are consistent with uncorrelated Eshelby transformations occurring along all orientations, in addition to the maximum shear directions. In the long-time displacement fields, the plastic strain along the direction of maximum shear dominates all others. Along the direction of maximum shear, the real-space strain correlations decay much more slowly than the Eshelby-like velocity correlations. Nonetheless, we find the same characteristic lengthscale setting a cutoff on the power spectrum along any particular direction.

For the pair drag dissipation mechanism we also found $D_e \sim \xi$, with both having similar rate dependance $\sim \dot{\gamma}^{-1/2}$. The $-1/2$ is stronger than the $-1/3$ from the mean drag dissipation. In [84], a length, l, was introduced to rationalize the rate dependence of D_e.

The relation $D_e \sim \xi$ (for $\xi << L$), remains the same here and can be understood as a simple kinematic consequence of plastic deformation essentially organizing along lines as in ref [84]. We have also established the connection between stress and particle diffusion via the effective Stoke-Einstein temperature. It seems to us that the emergence of a rate independent effective Stokes-Einstein temperature is a more compelling – and apparently general – connection between the diffusion and rheol-

ogy than a particular relationship between correlation length and stress relaxation time as in [84]. We further speculate that $D_e \delta\sigma$ may be related to various effective temperatures which arise in other mean-field and elasto-plastic models for amorphous plasticity.

In short, we have made a connection between the rheology, the diffusion coefficient, and the spatial correlations in the plastic strain in model jammed suspensions of soft particles. The excess stress, inverse effective diffusion and inverse correlation length are all governed by the HB exponent, $\sim \dot\gamma^\beta$. The two classes of dissipation, mean drag (appropriate for particles at an interface like bubble rafts) and pair drag (appropriate for particles in the bulk), give different β, but are otherwise virtually identical. Our main contribution has been to show the relation between these quantities in the two models. An a priori calculation of β in either the mean drag or pair drag case remains an outstanding problem.

In addition to the questions about the origin of the rate dependence of ξ and the relation between ξ and $\delta\sigma$, there are some other obvious open questions which needs to be understood in future. Can one reproduce our results in simple adaptations of the elasto-plastic models described in the introduction? What is the proper physical rationale for defining an effective temperature based on the excess stress rather than the total stress? Does one recover the same scaling laws when physical stress propagation happens in an inertial underdamped system? It would be quite interesting and relatively straightforward to include mass and modify the bubble model to study the role of inertia. These are some of the questions which will need to be addressed in the future in order to obtain a better understanding of these jammed suspensions

68

and a chance at constructing a first principles theory of their rheology.

Bibliography

[1] D. J. Durian, "Foam Mechanics at the Bubble Scale," *Physical Review Letters*, vol. 75, no. 26, pp. 4780–4783, 1995.

[2] W. Herschel and R. Bulkley, "Konsistenzmessungen von gummi-benzollösungen," *Kolloid Zeitschrift*, vol. 39, p. 291, 1926.

[3] V. J. Langlois, S. Hutzler, and D. Weaire, "Rheological properties of the soft-disk model of two-dimensional foams," *Physical Review E*, vol. 78, p. 21401, Aug. 2008.

[4] M. Cloitre, R. Borrega, F. Monti, and L. Leibler, "Structure and flow of poly-electrolyte microgels from suspensions to glasses," *Cr. Phys*, vol. 4, p. 221, 2003.

[5] E. Pratt and M. Dennin, "Nonlinear stress and fluctuation dynamics of sheared disordered wet foam," *Physical Review E*, vol. 67, no. 5, 2003.

[6] M. E. Möbius, G. Katgert, and M. van Hecke, "Relaxation and flow in linearly sheared two-dimensional foams," *EPL (Europhysics Letters)*, vol. 90, p. 44003, May 2010.

[7] K. N. Nordstrom, E. Verneuil, W. G. Ellenbroek, T. C. Lubensky, J. P. Gollub, and D. J. Durian, "Centrifugal compression of soft particle packings: Theory and experiment," *Physical Review E*, vol. 82, no. 4, pp. 1–8, 2010.

[8] J. R. Seth, L. Mohan, C. Locatelli-Champagne, M. Cloitre, and R. T. Bonnecaze, "A micromechanical model to predict the flow of soft particle glasses.," *Nature Materials*, vol. 10, pp. 838–43, Nov. 2011.

[9] G. Picard, a. Ajdari, F. Lequeux, and L. Bocquet, "Elastic consequences of a single plastic event: a step towards the microscopic modeling of the flow of yield stress fluids.," *Eur. Phys. J. E.*, vol. 15, pp. 371–81, Dec. 2004.

[10] C. E. Maloney and M. O. Robbins, "Evolution of displacements and strains in sheared amorphous solids," *J. Phys. Condens. Matter*, vol. 20, p. 244128, June 2008.

[11] C. E. Maloney and A. Lemaître, "Amorphous systems in athermal, quasistatic shear.," *Physical Review E*, vol. 74, p. 016118, July 2006.

[12] A. J. Liu, S. R. Nagel, W. Van Saarloos, and M. Wyart, "The jamming scenario-an introduction and outlook," *arXiv preprint arXiv:1006.2365*, 2010.

[13] C. S. O'Hern, L. E. Silbert, A. J. Liu, and S. R. Nagel, "Jamming at zero temperature and zero applied stress : The epitome of disorder," *Physical Review E*, vol. 68, p. 011306, 2003.

[14] C. S. O'Hern, "Random packings of frictionless particles," *Physical Review Letters*, vol. 88, no. 7, 2002.

[15] G. Katgert, B. P. Tighe, and M. van Hecke, "The jamming perspective on wet foams," *Soft Matter*, vol. 9, no. 41, p. 9739, 2013.

[16] C. P. Goodrich, S. Dagois-Bohy, B. P. Tighe, M. van Hecke, A. J. Liu, and S. R. Nagel, "Jamming in finite systems: Stability, anisotropy, fluctuations, and scaling," *Physical Review E*, vol. 90, p. 022138, Aug 2014.

[17] B. P. Tighe, "Relaxations and rheology near jamming," *Physical Review Letters*, vol. 107, no. 15, p. 158303, 2011.

[18] B. P. Tighe, "Critical viscoelastic response in jammed solids," *arXiv preprint arXiv:1205.2960*, 2012.

[19] G. Katgert, A. Latka, M. E. Möbius, and M. van Hecke, "Flow in linearly sheared two-dimensional foams: From bubble to bulk scale," *Physical Review E*, vol. 79, no. 6, p. 066318, 2009.

[20] G. Katgert, M. E. Möbius, and M. Van Hecke, "Rate dependence and role of disorder in linearly sheared two-dimensional foams," *Physical Review Letters*, vol. 101, no. 5, pp. 3–6, 2008.

[21] G. Katgert, B. P. Tighe, M. E. Möbius, and M. van Hecke, "Couette flow of two-dimensional foams," *EPL (Europhysics Letters)*, vol. 90, no. 5, p. 54002, 2010.

[22] V. Chikkadi, G. Wegdam, D. Bonn, B. Nienhuis, and P. Schall, "Long-Range Strain Correlations in Sheared Colloidal Glasses," *Physical Review Letters*, vol. 107, p. 198303, Nov. 2011.

[23] L. Mohan, M. Cloitre, and R. T. Bonnecaze, "Active microrheology of soft particle glasses," *Journal of Rheology*, vol. 58, pp. 1465–1482, Sept. 2014.

[24] A. Basu, Y. Xu, T. Still, P. E. Arratia, Z. Zhang, K. N. Nordstrom, J. M. Rieser, J. P. Gollub, D. J. Durian, and a. G. Yodh, "Rheology of soft colloids across the onset of rigidity: scaling behavior, thermal, and non-thermal responses.," *Soft matter*, vol. 10, no. 17, pp. 3027–35, 2014.

[25] L. Mohan, C. Pellet, M. Cloitre, and R. Bonnecaze, "Local mobility and microstructure in periodically sheared soft particle glasses and their connection to macroscopic rheology," *Journal of Rheology*, vol. 57, no. 3, p. 1023, 2013.

[26] L. Mohan, R. T. Bonnecaze, and M. Cloitre, "Microscopic Origin of Internal Stresses in Jammed Soft Particle Suspensions," *Physical Review Letters*, vol. 111, p. 268301, Dec. 2013.

[27] J. P. Sethna, K. A. Dahmen, and C. R. Myers, "Crackling noise," *Nature*, vol. 410, pp. 242–250, 2001.

[28] M. L. Falk and J. S. Langer, "Dynamics of viscoplastic deformation in amorphous solids," *Physical Review E*, vol. 57, pp. 7192–7205, June 1998.

[29] C. E. Maloney and A. Lemaitre, "Amorphous systems in athermal, quasistatic shear," *Physical Review E*, vol. 74, p. 16118, 2006.

[30] A. Tanguy, F. Leonforte, and J. L. Barrat, "Plastic response of a 2D Lennard-Jones amorphous solid: Detailed analysis of the local rearrangements at very slow strain rate," *European Physical Journal E*, vol. 20, pp. 355–364, 2006.

[31] K. E. Jensen, D. a. Weitz, and F. Spaepen, "Local shear transformations in deformed and quiescent hard-sphere colloidal glasses," *Physical Review E*, vol. 90, p. 042305, Oct. 2014.

[32] J.-L. Barrat and A. Lemaître, "Heterogeneities in amorphous systems under shear," *Dynamical Heterogeneities in Glasses, Colloids, and Granular Media*, vol. 150, p. 264, 2011.

[33] V. V. Bulatov and A. S. Argon, "A stochastic model for continuum elasto-plastic behavior. i. numerical approach and strain localization," *Modelling and Simulation Material Science and Engineering*, vol. 2, pp. 167–184, 1994.

[34] V. V. Bulatov and A. S. Argon, "A stochastic model for continuum elasto-plastic behavior. ii. numerical approach and strain localization," *Modelling and Simulation Material Science and Engineering*, vol. 2, pp. 185–202, 1994.

[35] V. V. Bulatov and A. S. Argon, "A stochastic model for continuum elasto-plastic behavior. iii. numerical approach and strain localization," *Modelling and Simulation Material Science and Engineering*, vol. 2, pp. 203–222, 1994.

[36] J. D. Eshelby, "The determination of the elastic field of an ellipsoidal inclusion, and related problems," *Proceedings of Royal Society*, vol. A 241, no. 376, 1957.

[37] M. Talamali, V. Petäjä, and D. Vandembroucq, "Strain localization and anisotropic correlations in a mesoscopic model of amorphous plasticity," *Comptes Rendus MÃ©canique*, vol. 340, pp. 275 – 288, 2012. Recent Advances in Micromechanics of Materials.

[38] J. Chattoraj and A. Lemaître, "Elastic Signature of Flow Events in Supercooled Liquids Under Shear," *Physical Review Letters*, vol. 111, p. 066001, Aug. 2013.

[39] A. Lemaître, "Structural Relaxation is a Scale-Free Process," *Physical Review Letters*, vol. 113, p. 245702, Dec. 2014.

[40] J. Chattoraj, *Effect of finite temperatures on the elementary mechanisms of plastic deformation in amorphous materials*. PhD thesis, Univ. Paris-Est, 2011.

[41] C. E. Maloney and M. O. Robbins, "Anisotropic power law strain correlations in sheared amorphous 2D solids.," *Physical Review Letters*, vol. 102, p. 225502, June 2009.

[42] A. S. Argon, "Plastic deformation in metallic glasses," *Acta Met*, vol. 27, p. 47, 1979.

[43] M. L. Falk and J. S. Langer, "Dynamics of viscoplastic deformation in amorphous solids," *Physical Review E*, vol. 57, no. 6, pp. 7192–7205, 1998.

[44] C. Maloney and A. Lemaître, "Universal Breakdown of Elasticity at the Onset of Material Failure," *Physical Review Letters*, vol. 93, p. 195501, Nov. 2004.

[45] C. Maloney and A. Lemaître, "Subextensive Scaling in the Athermal, Quasistatic Limit of Amorphous Matter in Plastic Shear Flow," *Physical Review Letters*, vol. 93, p. 016001, July 2004.

[46] A. Tanguy, F. Leonforte, and J. L. Barrat, "Plastic response of a 2d lennard-jones amorphous solid: Detailed analysis of the local rearrangements at very slow strain rate," *The European Physical Journal E*, vol. 20, no. 3, pp. 355–364, 2006.

[47] P. Hebraud and F. Lequeux, "Mode-Coupling Theory for the Pasty Rheology of Soft Glassy Materials," *Physical Review Letters*, p. 2934, 1998.

[48] E. Agoritsas, E. Bertin, K. Martens, and J.-l. Barrat, "On the relevance of disorder in athermal amorphous materials under shear," *arXiv:1501.04515 [cond-mat.soft]*, p. 1–23, 2015.

[49] P. Sollich, F. Lequeux, P. Hebraud, and M. E. Cates, "Rheology of Soft Glassy Materials," *Physical Review Letters*, no. 78, p. 2020, 1996.

[50] P. Sollich, "Rheological constitutive equation for a model of soft glassy materials," *Physical Review E*, vol. 58, no. 1, p. 24, 1997.

[51] A. Onuki, "Plastic flow in two-dimensional solids," *Physical Review E*, vol. 68, p. 61502, Dec. 2003.

[52] E. A. Jagla, "Strain localization driven by structural relaxation in sheared amorphous solids," *Physical Review E*, vol. 76, p. 46119, Oct. 2007.

[53] H. C. Lin, Y. H. Li, and C. Y. Chen, "Structural instability of an oscillating superparamagnetic micro-bead chain," *Microfluidics and Nanofluidics*, vol. 17, no. 1, pp. 73–84, 2014.

[54] J. Lin, A. Saade, E. Lerner, A. Rosso, and M. Wyart, "On the density of shear transformations in amorphous solids," *EPL (Europhysics Letters)*, vol. 105, p. 26003, Jan. 2014.

[55] A. Nicolas, K. Martens, L. Bocquet, and J.-L. Barrat, "Universal and non-universal features in coarse-grained models of flow in disordered solids.," *Soft matter*, vol. 10, no. 26, pp. 4648–61, 2014.

[56] E. R. Homer, D. Rodney, and C. A. Schuh, "Kinetic Monte Carlo study of activated states and correlated shear-transformation-zone activity during the deformation of an amorphous metal," *Physical Review B*, vol. 81, p. 64204, Feb. 2010.

[57] E. R. Homer and C. A. Schuh, "Mesoscale modeling of amorphous metals by shear transformation zone dynamics," *Acta Materialia*, vol. 57, pp. 2823–2833, May 2009.

[58] M. Talamali, V. Petäjä, D. Vandembroucq, and S. Roux, "Strain localization and anisotropic correlations in a mesoscopic model of amorphous plasticity," *Comptes Rendus Mécanique*, vol. 340, pp. 275–288, Apr. 2012.

[59] J. C. Baret, D. Vandembroucq, and S. Roux, "Extremal model for amorphous media plasticity," *Physical Review Letters*, vol. 89, p. 195506, Nov. 2002.

[60] D. Rodney, a. Tanguy, and D. Vandembroucq, "Modeling the mechanics of amorphous solids at different length scale and time scale," *Modelling and Simulation in Materials Science and Engineering*, vol. 19, p. 083001, Dec. 2011.

[61] D. Vandembroucq and S. Roux, "Mechanical noise dependent aging and shear banding behavior of a mesoscopic model of amorphous plasticity," *Physical Review B*, vol. 84, no. 13, pp. 1–6, 2011.

[62] M. Talamali, V. Petaejae, D. Vandembroucq, and S. Roux, "Avalanches, precursors, and finite-size fluctuations in a mesoscopic model of amorphous plasticity," *Physical Review E*, vol. 84, p. 16115, July 2011.

[63] C. Liu, E. E. Ferrero, F. Puosi, J. L. Barrat, and K. Martens, "Driving rate dependence of avalanche statistics and shapes at the yielding transition," *cond-mat-soft*, June 2015.

[64] E. Pratt and M. Dennin, "Nonlinear stress and fluctuation dynamics of sheared disordered wet foam.," *Physical Review E*, vol. 67, no. 5 Pt 1, p. 051402, 2003.

[65] G. Katgert, A. Latka, M. E. Mobius, and M. van Hecke, "Flow in linearly sheared two-dimensional foams: From bubble to bulk scale," *Physical Review E*, vol. 79, no. 6, p. 66318, 2009.

[66] M. E. Möbius, G. Katgert, and M. van Hecke, "Relaxation and flow in linearly sheared two-dimensional foams," *EPL (Europhysics Letters*, vol. 90, no. 44003, 2008.

[67] G. Katgert, B. P. Tighe, M. E. Möbius, and M. van Hecke, "Couette flow of two-dimensional foams," *EPL (Europhysics Letters)*, vol. 90, no. 5, p. 54002, 2010.

[68] S. Plimpton, "Fast parallel algorithms for short-range molecular dynamics," *Journal of Computational Physics*, vol. 117, no. 1, pp. 1 – 19, 1995.

[69] M. P. Allen and D. J. Tildesley, *Computer Simulation of Liquids.* Oxford Science Publications, 1989.

[70] J. H. Irving and J. G. Kirkwood, "The statistical mechanical theory of transport processes. iv. the equations of hydrodynamics," *Journal of Chemical Physics*, vol. 18, pp. 817–829, 1950.

[71] M. C. Miguel, A. Vespignani, S. Zapperi, J. Weiss, and J.-R. Grasso, "Intermittent dislocation flow in viscoplastic deformation," *Nature*, vol. 410, pp. 667–671, 04 2001.

[72] M. Zaiser and N. Nikitas, "Slip avalanches in crystal plasticity: scaling of the avalanche cut-off," *Journal of Statistical Mechanics: Theory and Experiment*, vol. 2007, no. 04, p. P04013, 2007.

[73] S. Zapperi, A. Vespignani, and H. E. Stanley, "Plasticity and avalanche behaviour in microfracturing phenomena," *Nature*, vol. 388, pp. 658–660, 08 1997.

[74] S. Zapperi, C. Castellano, F. Colaiori, and G. Durin, "Signature of effective mass in crackling-noise asymmetry," *Nature Physics*, vol. 1, pp. 46–49, 10 2005.

[75] C. R. Myers and J. P. Sethna, "Collective dynamics in a model of sliding charge-density waves. i. critical behavior," *Physical Review B*, vol. 47, pp. 11171–11193, May 1993.

[76] O. Perković, K. Dahmen, and J. P. Sethna, "Avalanches, barkhausen noise, and plain old criticality," *Physical Review Letters*, vol. 75, pp. 4528–4531, Dec 1995.

[77] J. P. Sethna, K. A. Dahmen, and C. R. Myers, "Crackling noise," *Nature*, vol. 410, pp. 242–250, 03 2001.

[78] S. Tewari, D. Schiemann, D. J. Durian, C. M. Knobler, S. a. Langer, and a. J. Liu, "Statistics of shear-induced rearrangements in a two-dimensional model foam.," *Physical Review E*, vol. 60, no. 4 Pt B, pp. 4385–4396, 1999.

[79] J. Lin, E. Lerner, A. Rosso, and M. Wyart, "Scaling description of the yielding transition in soft amorphous solids at zero temperature," *Proceedings of the National Academy of Sciences*, vol. 111, no. 40, pp. 14382–14387, 2014.

[80] K. M. Salerno, C. E. Maloney, and M. O. Robbins, "Avalanches in Strained Amorphous Solids: Does Inertia Destroy Critical Behavior?," *Physical Review Letters*, vol. 109, p. 105703, Sept. 2012.

[81] K. Salerno and M. Robbins, "Effect of inertia on sheared disordered solids: Critical scaling of avalanches in two and three dimensions," *Physical Review E*, vol. 88, p. 062206, Dec. 2013.

[82] E. Lerner and I. Procaccia, "Locality and nonlocality in elastoplastic responses of amorphous solids," *Physical Review E*, vol. 79, p. 066109, Jun 2009.

[83] G. Picard, A. Ajdari, F. Lequeux, and L. Bocquet, "Elastic consequences of a single plastic event: A step towards the microscopic modeling of the flow of yield stress fluids," *European Physical Journal E*, vol. 15, pp. 371–381, 2004.

[84] A. Lemaitre and C. Caroli, "Rate-Dependent Avalanche Size in Athermally Sheared Amorphous Solids," *Physical Review Letters*, vol. 103, no. 6, p. 65501, 2009.

[85] A. Lemaitre and C. Caroli, "Plastic response of a two-dimensional amorphous solid to quasistatic shear: Transverse particle diffusion and phenomenology of dissipative events," *Physical Review E*, vol. 76, p. 36104, Sept. 2007.

[86] C. E. Maloney and M. O. Robbins, "Evolution of displacements and strains in sheared amorphous solids," *Journal of Physics-Ccondensed Matter*, vol. 20, p. 244128, June 2008.

[87] J. Chattoraj, C. Caroli, and A. Lemaître, "Robustness of avalanche dynamics in sheared amorphous solids as probed by transverse diffusion," *Physical Review E*, vol. 84, p. 011501, July 2011.

[88] I. K. Ono, C. S. O'Hern, D. J. Durian, S. A. Langer, A. J. Liu, and S. R. Nagel, "Effective temperatures of a driven system near jamming," *Physical Review Letters*, vol. 89, 2002.

[89] I. K. Ono, S. Tewari, S. A. Langer, and A. J. Liu, "Velocity fluctuations in a steadily sheared model foam," *Physical Review E*, vol. 67, p. 61503, June 2003.

Appendix A

Non-affine Displacement Calculation for Oblique Cell

At first real space particle positions (x_i, y_i) are exported from LAMMPS simulation, within a single **Bravais cell**, described by the Bravais vectors, $\vec{d_1}$ and $\vec{d_2}$. The positions of all particles are represented by real-space co-ordinates that lie on the interior of the parallelogram defined by $\vec{d_1}$ and $\vec{d_2}$. Note that the Bravais vectors for a certain configuration are expressed with the cartesian unit vectors (in 2D) as,

$$\vec{d_1} = |d_1|\hat{x} \tag{A.1}$$

$$\vec{d_2} = |d_2|(\sin\theta\hat{x} + \cos\theta\hat{y}) \tag{A.2}$$

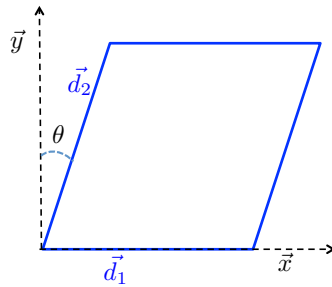where, $|d_1| = |d_2|\cos\theta = L$, size of the square simulation box before imposing the strain.

Figure A.1: Bravais Cell representation

Numerically, the value of strain (γ) is usually kept in the interval of (-0.5, 0.5]. For $\gamma = 0.5$, the symmetry in the system is utilized and the triangular right half is

transposed to the left side of the system, This is known as the **T-transformation**. Due to this, the orientation of the cell depends on the amount of the strain experienced; after every odd multiple of the half strain the slope of the director line changes from +0.5 to -0.5.

For each pair of times $\{t_1, t_2\}$ for which a displacement calculation is required, the position at t_1 is subtracted from the position at t_2 and a minimum image convention is applied to the difference to account for the transit of a particle across the cell boundary between t_1 and t_2. In this way, the the total displacement incurred between the time interval of $\Delta t = t_2 - t_1$ is obtained,

$$
\begin{aligned}
u_{i,x}^{T}(\Delta t) &= x_i(t_2) - x_i(t_1) & \text{(A.3)} \\
u_{i,y}^{T}(\Delta t) &= y_i(t_2) - y_i(t_1) & \text{(A.4)}
\end{aligned}
$$

Next, the affine displacement field is subtracted off from the total displacement,

$$
\begin{aligned}
u_{i,x}(\Delta t) &= u_{i,x}^{T}(\Delta t) - \left[\frac{y_i(t_1) + y_i(t_2)}{2} \right] \dot{\gamma} \Delta t & \text{(A.5)} \\
u_{i,y}(\Delta t) &= u_{i,y}^{T}(\Delta t) & \text{(A.6)}
\end{aligned}
$$

Note that this procedure removes the affine motion corresponding to the average of the initial and final positions. In practice, one should compute non-affine displacement at long time by adding the non-affine displacements occurring on short time intervals. Finally the displacement data are associated with the particle positions at time $1(t_1)$ into the primary Bravais cell: x and y-displacement of 'i'-th particle at time t_1 with real space co-ordinates $(x_i(t_1), y_i(t_1))$ is denoted by $u_{i,x}(t_1, \Delta t)$ and $u_{i,y}(t_1, \Delta t)$ respectively.
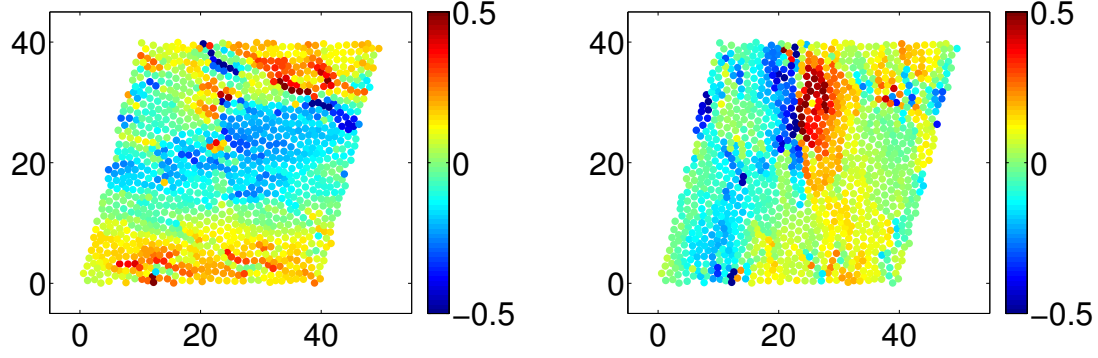
Figure A.2: Displacement occurred in a strain interval ($\Delta\gamma$) of 2.5% for each particle; Left: $u_{i,x}$ and Right: $u_{i,y}$.

An oblique grid$[N_g, N_g]$ with a spacing of $d = 1/2$, in x-direction (such that $L/d = N_g$) is created on our cell, which excludes the top and right boundary to maintain periodicity. A grid point or a particular node in our oblique mesh is denoted by the (m,n) pair indices, where $m, n \in [1, N_g]$

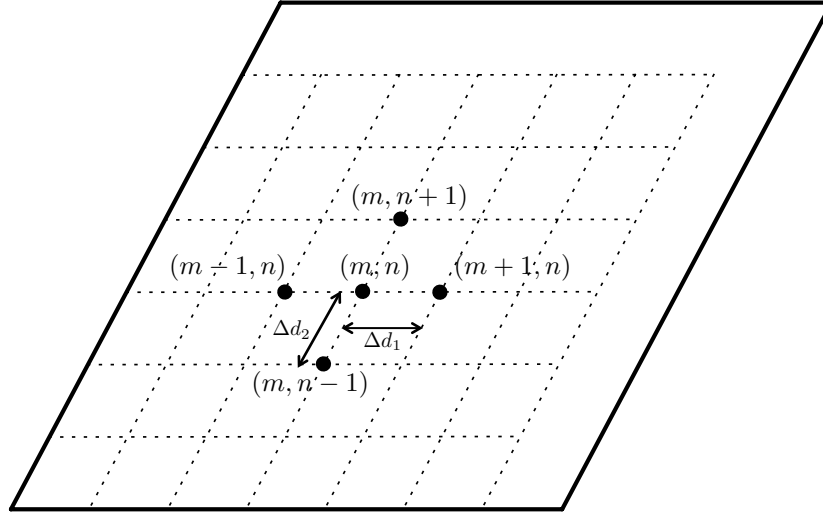Figure A.3: Oblique mesh mapped onto the Bravais cell. The real space co-ordinate at a particular node (m,n) is denoted by $(x_{m,n}, y_{m,n})$.

In order to interpolate the displacement data onto this grid a cell with sufficiently larger dimensions(precisely 10% longer on each direction) than the Bravais cell is considered, which captures our cell symmetrically inside in it. Then the area outside

the cell is populated with the appropriate image particles containing the previously computed displacement data.At last the displacement data is linearly interpolated onto the mesh such that $u_x(m,n)$ denotes the magnitude of the x-displacement at the node(m,n) on our oblique mesh.
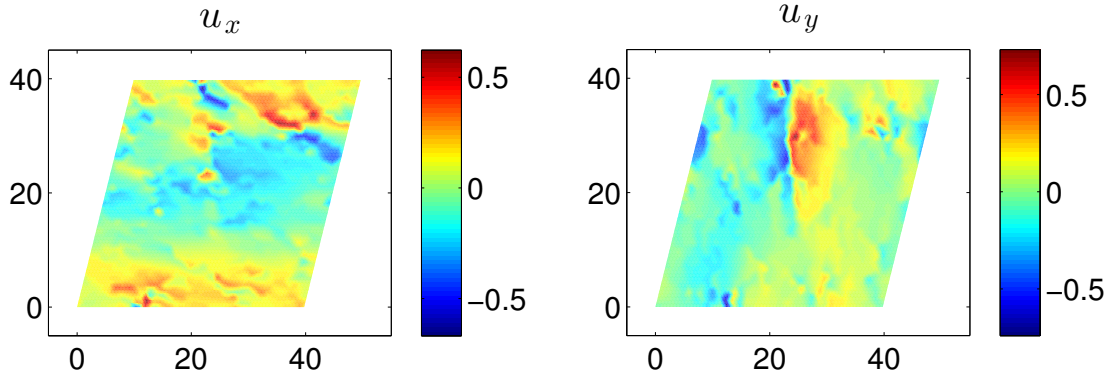

Figure A.4: Interpolated displacement field, u_x(left) and u_y(right) onto our oblique grid.

Appendix B

Numerics for Gradient Calculation on an Oblique Cell

To calculate the gradients of a scalar field in 2D rectilinear space, the approach of calculating it along the Bravais vector direction $(\vec{d_1}, \vec{d_2})$ is taken and then it is transformed back to the Cartesian direction$(\vec{x}, \vec{y})$. We can express the Bravais unit vectors as,

$$
\begin{aligned}
\hat{d}_1 &= \hat{x} & \text{(B.1)} \\
\hat{d}_2 &= \sin\theta\hat{x} + \cos\theta\hat{y} & \text{(B.2)}
\end{aligned}
$$

The equivalent gradient operator can be defined for these two co-ordinate systems as,

$$
\begin{aligned}
\nabla &= \hat{x}\frac{\partial}{\partial x} + \hat{y}\frac{\partial}{\partial y} & \text{(B.3)} \\
&= \hat{d}_1\frac{\partial}{\partial d_1} + \hat{d}_2\frac{\partial}{\partial d_2} & \text{(B.4)}
\end{aligned}
$$

where, $\frac{\partial}{\partial d_1} = \hat{d}_1.\nabla$ and $\frac{\partial}{\partial d_2} = \hat{d}_2.\nabla$

Mapping the gradient in Bravais space to Rectilinear space

The cartesian derivative operator can be obtained in terms of the new derivative operator,

$$
\begin{bmatrix} \frac{\partial}{\partial x} \\[2mm] \frac{\partial}{\partial y} \end{bmatrix} = \begin{bmatrix} 1 & 0 \\[2mm] -\tan\theta & \sec\theta \end{bmatrix} \begin{bmatrix} \frac{\partial}{\partial d_1} \\[2mm] \frac{\partial}{\partial d_2} \end{bmatrix} \tag{B.5}
$$

where, θ is the angle $\vec{d_2}$ makes with the vertical in an anti-clockwise direction. In the numerical scheme, finite difference approach is taken to calculate the derivative along $\vec{d_1}, \vec{d_2}$ for any scalar field ϕ defined on oblique grid. For any grid-point inside the Bravais cell, the **central difference** is used,

$$
\left(\frac{\partial \phi}{\partial d_1} \right)_{m,n} = \frac{\phi(m+1,n) - \phi(m-1,n)}{2\Delta d_1} \tag{B.6}
$$

$$
\left(\frac{\partial \phi}{\partial d_2} \right)_{m,n} = \frac{\phi(m,n+1) - \phi(m,n-1)}{2\Delta d_2} \tag{B.7}
$$

where $\Delta d_1 = (x_{m+1,n} - x_{m,n})$ and $\Delta d_2 = \sqrt{(x_{m,n+1} - x_{m,n})^2 + (y_{m,n+1} - y_{m,n})^2}$. Periodic boundary conditions are used for all boundary nodes.

Using equation B.5, the gradients of ϕ with respect to the cartesian orthogonal directions is acquired.

Appendix C

Power spectrum for scalar field

The Fourier space representation of the real space function $\phi(\vec{r})$ is obtained by the decomposition of the function into its Fourier modes, which can also be seen as the series sum,

$$\phi(\vec{r}) = \sum_{\vec{k}} \tilde{\phi}(\vec{k}) e^{i\vec{k}.\vec{r}} \tag{C.1}$$

where $\vec{k}$ lies on the reciprocal lattice $[\vec{k} = p_1\vec{b_1} + p_2\vec{b_2}$, with p_1, p_2 as arbitrary integers] of the primary Bravais cell $[\vec{R} = n_1\vec{d_1} + n_2\vec{d_2}$, with n_1, n_2 as arbitrary integers] that satisfies,

$$\vec{d_i}.\vec{b_j} = 2\pi\delta_{ij} \tag{C.2}$$

Discrete Fourier Transform operator ($\mathcal{F}$)

$\tilde{\phi}$ is attained by taking the Discrete Fourier Transform (DFT) of ϕ via the operator $\mathcal{F}$.

$$\mathcal{F}(\phi(\vec{r})) = \sum_{\vec{r}} \phi(\vec{r}) e^{-i\vec{k}.\vec{r}} = \tilde{\phi}(\vec{k}) \tag{C.3}$$

$$\mathcal{F}^{-1}(\tilde{\phi}(\vec{k})) = \sum_{\vec{k}} \tilde{\phi}(\vec{k}) e^{i\vec{k}.\vec{r}} = \phi(\vec{r}) \tag{C.4}$$

We use FFT algorithm to perform the DFT on our scalar data $\phi(m,n)$ defined on the oblique mesh. The 2-dimensional DFT of ϕ can be represented as,

$$\tilde{\phi}(p,q) = \sum_{m=1}^{N_g}\sum_{n=1}^{N_g} \phi(m,n) e^{-2\pi i\left(\frac{(m-1)(p-1)}{N_g} + \frac{(n-1)(q-1)}{N_g}\right)} \tag{C.5}$$

where, (p, q) are the fourier indices of a grid-point in the reciprocal space satisfying $p, q \in [1, N_g]$.

Mapping the DFT data in reciprocal space

The next step is to represent our transformed data onto a regular mesh in the Fourier space. Using equaltions A.1 and C.2, we derive the expression of the physical wave vectors,

$$\vec{b_1} = \frac{2\pi}{L}\left(\hat{x} - \tan\theta\hat{y}\right) \tag{C.6}$$

$$\vec{b_2} = \frac{2\pi}{L}\hat{y} \tag{C.7}$$

The wave number in the reciprocal space corresponding to the fourier indices(p, q) is given by,

$$k_x(p, q) = \frac{2\pi}{L}(p) \tag{C.8}$$

$$k_y(p, q) = \frac{2\pi}{L}(q - p\tan\theta) \tag{C.9}$$

In this way we map discrete data, $\tilde{\phi}(p, q)$ on the Fourier space and obtain $\tilde{\phi}(k_x, k_y)$.

Average on various Bravais orientation

Fourier space calculation is performed for $\phi^t(x, y)$ on different time instant(t) and $\tilde{\phi}^t(k_x, k_y)$ is obtained. A rectangular grid $\left[\frac{N_g}{2} + 1, \frac{N_g}{2} + 1\right]$ is drawn on our reciprocal space(r, s) such that $r, s \in \left[-\frac{N_g}{4}, \frac{N_g}{4}\right]$ and simultaneously $\frac{k_x}{2\pi}, \frac{k_y}{2\pi} \in \left[-1, 1\right]$. For each configuration t then $\tilde{\phi}(k_x, k_y)$ is linearly interpolated on that grid. Finally it is averaged over different configurations to get the power spectrum of $\tilde{\phi}(k_x, k_y)$ as:

$$|\tilde{\phi}(\vec{k})|^2 = \langle|\tilde{\phi}^t(k_x, k_y)|^2\rangle_t \tag{C.10}$$

At the last step, the power spectrum is normalized with suitable quantity to represent the structure factor in 2D space.

$$S_\phi(\vec{k}) = \frac{1}{N_g^2}\frac{|\tilde{\phi}_x(\vec{k})|^2}{\langle\vec{\phi}\cdot\vec{\phi}\rangle} \tag{C.11}$$